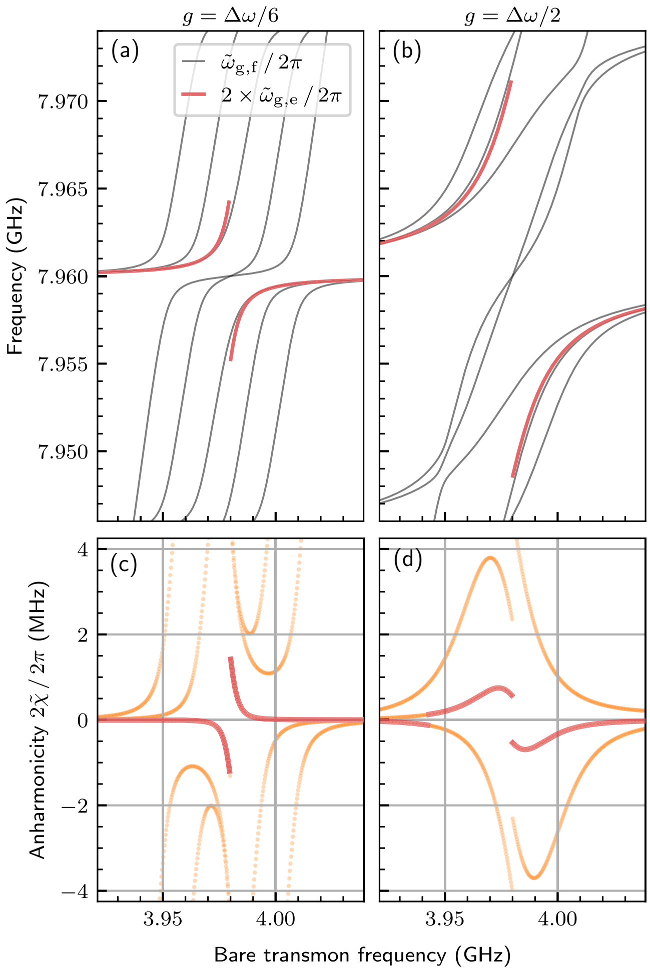

FIG. 9. Two-excitation subspace and anharmonicities. Simulations use the same model as in Fig. 7. (a) and (b) Part of the two-excitation energy levels $\tilde{\omega}_{g,f} / 2\pi$ (gray lines) zoomed-in around twice the single ground state transition energy $2 \times \tilde{\omega}_{g,e} / 2\pi$ of the central acoustic mode (red). (c) and (d) Anharmonicities $2\tilde{\chi} / 2\pi$ associated to the red hybrid mode of Figs. 7(a) and 7(b) within ± 4 GHz are shown with orange circle markers. The smallest (in absolute value) anharmonicity is shown with a thick red line and corresponds to the anharmonicity shown in Figs. 7(c) and 7(d).

qubit is $2\chi_{\rm tr}/2\pi = -E_{\rm C}/h = -200$ MHz, corresponding to a typical transmon qubit [90]. We consider a uniform coupling between transmon and acoustic modes, with a single-mode coupling regime $g = \Delta\omega/6 = 2\pi \times 2.5$ MHz, and a multimode coupling regime $g = \Delta\omega/2 = 2\pi \times 7.5$ MHz. The single-excitation energy levels $\omega_{g,e}$ are reported in Figs. 7(a) and 7(b). The two-excitation energy spectrum contains 21 levels, part of which is shown with gray solid lines in Figs. 9(a) and 9(b). The red line shows twice the single-excitation energy of the red hybrid mode of Figs. 7(a) and 7(b), which corresponds mainly to the central acoustic mode with bare frequency 3.98 GHz. To define the anharmonicity of this hybrid mode, we compute the frequency differences $2\tilde{\chi} = \tilde{\omega}_{e,f} - \tilde{\omega}_{g,e}$ for all two-excitation levels $\tilde{\omega}_{e,f}$, i.e., half the difference between the red line and all gray lines. We thus get several anharmonicities $2\tilde{\chi}$ (21 for 5 acoustic modes). The one within ± 4 MHz are reported in Figs. 9(c) and 9(d) with orange markers. The smallest absolute anharmonicity per bare transmon frequency is shown with a thicker red line, and corresponds to the value shown in Figs. 7(c) and 7(d). Some of the transitions may have zero matrix elements, but we consider the most stringent case by including all transitions.

A hybrid mode can be considered a qubit if its smallest anharmonicity (by magnitude) is much larger than its decoherence rate. However, to be considered a *mechanical* qubit, it should have a weak bare qubit participation ratio $|u_{\rm tr}|^2$. To identify mechanical qubits in Fig. 7, we decompose the hybrid modes in the bare mode basis, as shown in Fig. 10. The bare qubit participation is shown with black dashed lines, and we only consider hybrid modes with participation weaker than $|u_{\rm tr}|^2 < 20\%$.

d. Effect of transmon qubit dissipation rate

In Fig. 7, we assumed a moderate total dissipation rate for the transmon qubit, $\kappa_{\rm tr}/2\pi = 300$ kHz, which is consistent with values reported in the literature for direct fabrication of transmons on GaAs [16]. However, this value is lower than what we measured for the SQUID array resonator in this work, $\kappa_{\rm SQ,int}^{\rm extra}/2\pi = 2$ MHz (Fig. 18). We numerically investigated the impact of the transmon qubit dissipation rate on the number of mechanical qubits, fixing all the others parameters as in Fig. 7. For $\kappa_{\rm tr}/2\pi = 600$ kHz, we still obtain four mechanical qubits over an extended range of bare transmon frequencies. For $\kappa_{\rm tr}/2\pi = 1000$ kHz, three mechanical qubits remain accessible. At $\kappa_{\rm tr}/2\pi = 1500$ kHz, only a single mechanical qubit can be realized; however, it is possible to recover four simultaneous mechanical qubits by increasing both the coupling strength g and the FSR.

The dissipation rate of the transmon qubit can be further reduced by using a flip-chip integration technique [93–95], where all components except the transmon qubit are fabricated on GaAs, and the qubit is fabricated on a silicon or sapphire substrate. Such architectures have been experimentally demonstrated, yielding transmon qubit lifetimes of $\approx 10\,\mu$s [94]. In Fig. 11, we assume a compatible transmon decoherence rate of $\kappa_{\rm SQ}/2\pi = 2\Gamma_2/2\pi = 25$ kHz. We also assume reduced SAW dissipation rates, setting $\kappa/2\pi = 25$ kHz, which has been demonstrated on similar GaAs substrates with optimized IDT and Bragg mirror designs [28].

e. Optimizing the number of mechanical qubits

We note that increasing the coupling g excessively can be detrimental to the realization of multiple mechanical qubits. In fact, in this regime, the transmon participation

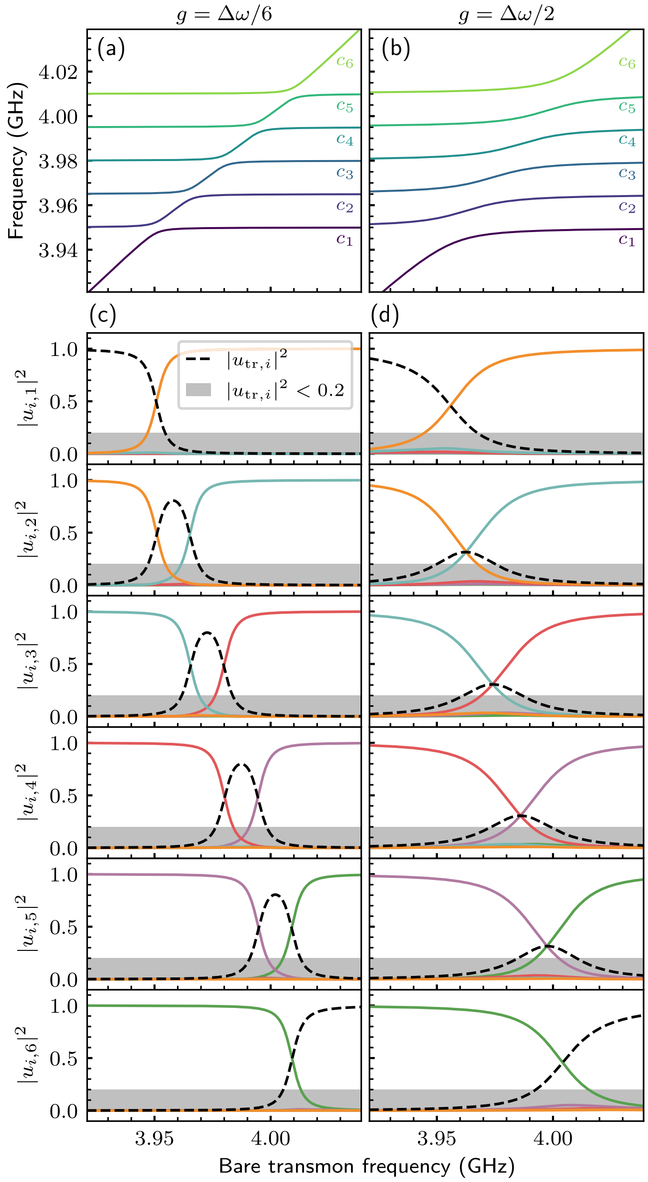

FIG. 10. Bare modes participation in hybrid qubits. Simulations use the same model as in Fig. 7. (a) and (b) The single-excitation energy spectrum is reproduced from Figs. 7(a) and 7(b). Each color corresponds to a different hybrid mode from c_1 to c_6. (c) and (d) Hybrid modes decomposition in the bare mode basis. Each row corresponds to the decomposition of one hybrid mode of (a) and (b). The bare transmon participation ratio is shown in black dashed lines, while the participation of other bare acoustic modes is shown with colored solid lines. The area shaded in gray corresponds to hybrid modes with transmon participation under 20 %, which we classify as mainly mechanical.

in the hybrid modes becomes vanishingly small, except for the first and last hybrid modes of the passband, which retain substantial transmon participation. This behavior is akin to the formation of atom-photon bound states in systems with dispersion relations featuring band gaps [96]. Therefore, the coupling g should be kept smaller than

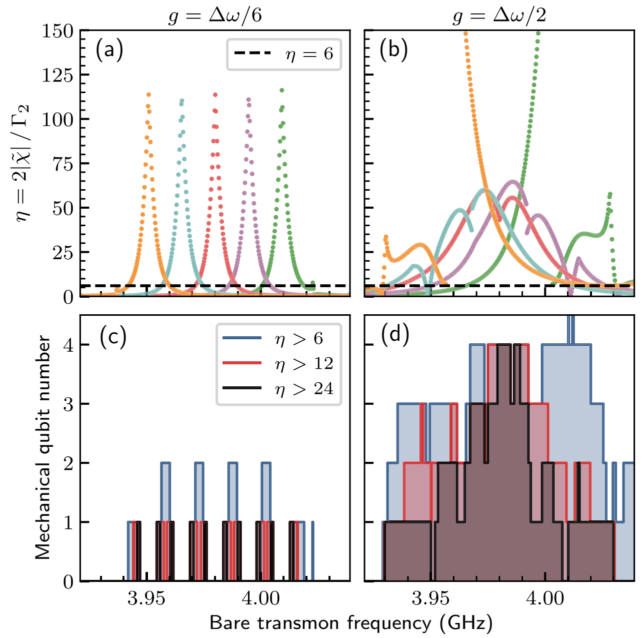

FIG. 11. Simulations for mechanical qubits with reduced dissipation rates. Simulations use the same model as in Figs. 7(e)–7(h), but with reduced total dissipation rates $\kappa_{\mathrm{SQ}}/2\pi = \kappa/2\pi = 25\,\mathrm{kHz}$, compatible with a flip-chip architecture. Compared to Fig. 7, the nonlinearity to decoherence ratios are larger [(a) and (b)], enabling mechanical qubits over a broader range of bare transmon frequencies and with larger nonlinearity to decoherence ratios [(c) and (d)].

the SAW cavity bandwidth to realize multiple mechanical qubits.

The transmon qubit anharmonicity can also be optimized to maximize the number of mechanical qubits. In the regime where $\chi_{\mathrm{tr}} \gg g$, the anharmonicity of the hybrid modes is primarily determined by g. However, by carefully selecting χ_{tr} to be moderate, one can access a straddling regime [81] in which the hybrid modes retain significant anharmonicity over a wider range of bare transmon frequencies, potentially increasing the number of mechanical qubits. Conversely, if χ_{tr} is too large, the transmon's second transition frequency ω_{ef} is very detuned from the bare SAW mode frequencies, thereby limiting the effectiveness of the straddling regime. For the parameters used in Fig. 7, we find that $\chi_{\mathrm{tr}}/2\pi = -100\,\mathrm{MHz}$ offers a good compromise.

APPENDIX C: EXPERIMENTAL DETAILS: DESIGN, FABRICATION, SETUP

1. Fabrication

The fabrication begins with a cleansing of an intrinsic semi-insulating gallium arsenide wafer (AXT Inc) in isopropanol (IPA).

a. Interdigital transducer (IDT)

The 2" GaAs substrate is spin-coated with a double-resist layer of 60 nm of methyl methacrylate (MMA) followed by 100 nm poly methyl methacrylate (PMMA). Both layers are baked at 180 °C for 5 min. The crystallographic direction [100] is aligned in the microscope with a precision of $\pm 0.5^\circ$, and mounted on the cassette of an E-beam lithography machine (Raith EBPG 5200). The IDTs are exposed with a beam of 2 nA and a base dose of 250 $\mu C/cm^2$, proximity error correction and with 20 nm negative bias on the fingers' width. After developing the resist in a solution of MIBK:IPA 1:1 for 60 s the wafer is blow dry with a nitrogen gun and exposed to 10 s oxygen plasma generated with 50 W of power (Plasma-Therm). The sample is loaded in the evaporation chamber of a Plassys evaporator and pumped overnight to reach a base pressure of 5×10^{-8} mBar. Following the evaporation of 30 nm thick layer of aluminum, the wafer is placed in a preheated beaker with Rem1165 at 85 C for 30 min and left in lift-off for additional 3 h. After the aluminum residues have been removed with a pipette, the wafer is transferred to a new beaker with Rem 1165 at 85 C for 5 min, followed by sonication at 40% power at 35 kHz for 3 min. The same operation is repeated after transferring the wafer to room-temperature methanol and finally to a beaker with room-temperature IPA.

b. Ground plane

The wafer is spin-coated with double-layer optical resist, 300 nm of LOR 3A, baked at 180C for 5 min and 500 nm of S1805, baked at 115C for 5 min. The resist is exposed with 97 mJ/cm^2, developed in MF319 for 60 s with a light manual agitation and rinsed with a deionized water gun for 2 min. After a light descum in oxygen plasma at 20 W for 20 s the wafer is loaded in Plassys evaporator where 150 nm of aluminum are deposited. For lift-off we follow the same procedure used for the IDT.

c. Josephson junctions

The wafer is spin-coated with double-resist layer comprising 400 nm of MMA and 400 nm of PMMA and both layers are baked at 180 C for 5 min. The exposure Manhattan junctions pattern is performed in the electron beam lithography (EBL) with a dose of 600 $\mu C/cm^2$, and is followed by a development of 60 s in a solution of MIBK:IPA 1:1 and a light descum in oxygen plasma at 50 W for 20 s. The wafer is loaded in a Plassys evaporator where 50 nm of aluminum is deposited at 45° angle, followed by a static oxidation at 2 mBar for 20 min. After rotating the wafer axially by 90°, another deposition of 110 nm of aluminum is performed. Before venting the loadlock, the wafer is left 10 min in 10 mBar oxygen atmosphere.

d. Patches

To patch the junctions and the IDT to the ground plane we coat, expose and develop the pattern with the same procedure followed for the junctions. In the evaporator the wafer is exposed to Argon milling at 400 V for 2 min, followed by an evaporation of 200 nm of aluminum and by an oxidation in 10 mBar atmosphere for 10 min. Finally the standard lift-off procedure is performed.

As a final remark, the fabrication of the measured sample was performed in October 2020. From measurements performed on nominally identical samples right after the fabrication, we noticed negligible ageing in the chip performance. However, holes of hundreds of μm^2, clearly visible by optical microscopy, appeared on the large aluminum ground-pad.

2. Measurement setup

The measurement setup is shown in Fig. 12. The sample is wire bonded with aluminum wires on a custom printed circuit board and glued on a copper sample holder using PMMA resist. The sample holder is thermally anchored to the mixing chamber plate of a LD Bluefors cryostat with base temperature $\approx$10 mK. The sample holder is isolated from its electromagnetic environment via a shield with three layers: copper, aluminum and cryoperm.

Measurement signals are generated using a Quantum Machines platform comprising an arbitrary waveform generator (OPX+) and a frequency converter (octave). The output lines 1 and 2 of the octave are connected to the device via respectively the port 3 (launcher IDT feedline) and port 1 (SQUID array resonator feedline input) with nominally 70 dB attenuation. The transmission through the SQUID array feedline is collected from port 2 of the device and is amplified by a HEMT LNF-LNC4 8C at the 4 K stage. The reflected SAW feedline signal is measured using a circulator LNF-CICIC4 8A, and is also amplified by a HEMT LNF-LNC4 8C at the 4 K stage. A Marki FLP-0490 4.9 GHz low-pass filter is used on the port 1 of the device. Two double-isolators LNF-CICIC4 8A are used between device and HEMT. The signal is further amplified at room temperature using an Agile AMT-A0284 amplifier, and demodulated and downconverted in the Quantum Machines system.

The flux line of the SQUID array is connected to two coaxial lines via a Mini-Circuits ZDSS-2R5G5G-S+ diplexer, with each line including 30 dB of attenuation. A high-frequency line with a Mini-Circuits VHF-6010+ high-pass filter is used to apply the two-photon parametric drive. A low-frequency line with a Mini-Circuits VLFX-225+ low-pass filter is connected but not used in this work. An additional 10 dB of attenuation is inserted between the device and the diplexer to damp standing-wave modes.

Throughout this work, the bare frequency of the SQUID array is controlled using a superconducting coil attached

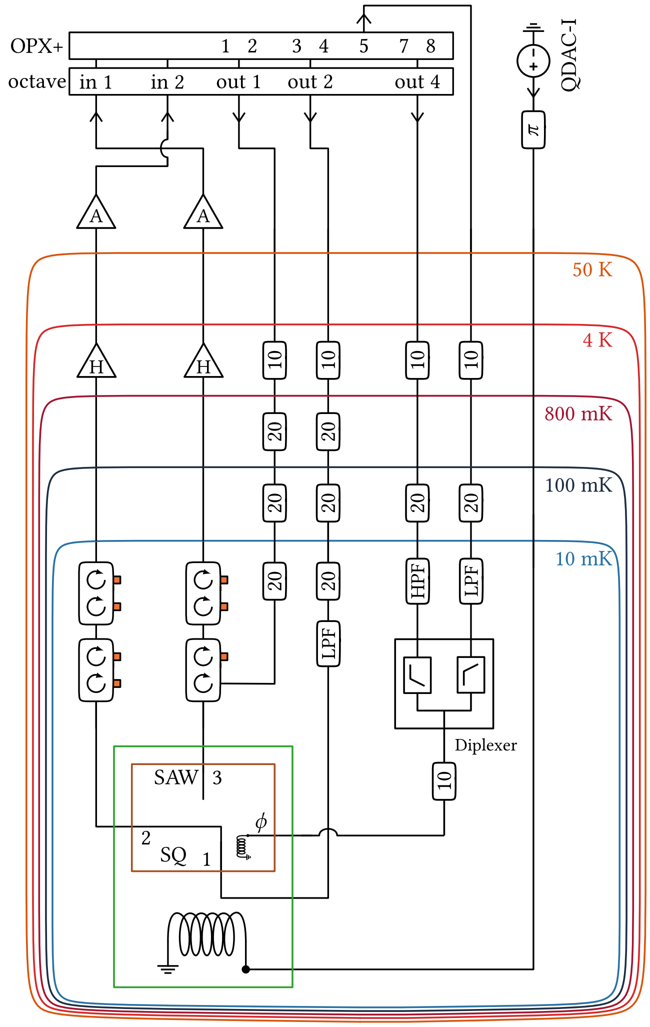

FIG. 12. Room-temperature measurement setup and cryostat wiring and filtering. Representative measurement setup used in cooldown 20251031CD. Minor changes performed in the other cooldowns are described in Sec. C 3.

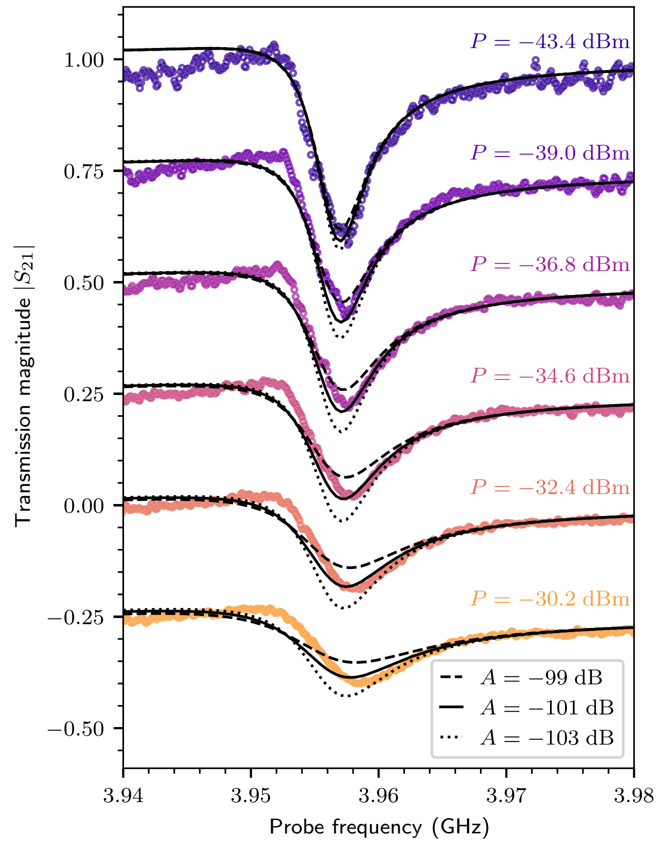

FIG. 13. Input line attenuation calibration. We perform a power sweep on a different device to calibrate the attenuation in the input line of the SQUID array resonator (port 1). The device is a Kerr resonator with nonlinearity exceeding its total dissipation rate studied in another work (device $N = 10$ in Ref. [66]). The colored markers indicate the magnitude of S_{21} measured for different powers P indicated at instrument level outside of the cryostat. Each S_{21} trace is shifted along y-axis by -0.25. We use the method described in Ref. [66] and fit the power sweep to a master equation model using QuTiP [92]. We find an attenuation of -101 ± 1 dB (black solid line). Dashed and dotted black lines indicate simulation results with ± 2 dB attenuation difference and show a worse agreement with the measurements.

on the bottom of the sample holder. We use a QDevil QDAC-I voltage source with a 1 kΩ low-pass π-filter with 30 Hz cutoff frequency to apply direct current in the coil.

3. Attenuation estimation

The measurement data reported in this work were measured across several CDs. In one cooldown (CD 20241206), we performed a calibration of the input attenuation line of the SQUID array resonator (port 1) using another device connected on a shared cryogenic switch at the mixing chamber stage of the cryostat. It is a Kerr resonator in the quantum regime, i.e., with nonlinearity larger than dissipation. The nonlinearity is known from the measurement of multiphoton transitions at high probe power [66]. We fit the power sweep shown in Fig. 13 with the input attenuation as the only free parameter. The Kerr resonator device and input power calibration method are explained in greater details in Ref. [66]. This allows us to find the self-Kerr χ_{SQ} of the SQUID array resonator presented in this work as reported in Fig. 5. The input line connected to port 3 (launcher IDT) is nominally identical to the one connected to port 1. We determine the attenuation of the launcher IDT input line by using the attenuation calibrated for port 1, accounting for difference in filtering and cabling at the mixing chamber stage of the cryostat using nominal room-temperature values for the different microwave components.

We recalibrate the attenuation of the input lines for all the other cooldowns, according to the following procedure:

CD 20241206; During this cooldown, port 1 (input of the SQUID array resonator feedline) is connected on the same switch as the Kerr resonator [66]. The input attenuation is calibrated using the method described above, and we find $A_3{}^{SQ} = (-101 \pm 1)$ dB.

In the other cooldowns, no switch was used on the SQUID array resonator input (port 1), and the estimate of the attenuation of the input lines is based on the calibration performed during CD 20241206, given that the lines are nominally the same.

CD 20240913; We estimate the attenuation in the launcher IDT feedline by subtracting the nominal room-temperature attenuation of the additional components used in CD 20241206, namely

(a) one Marki LPF 4.9 GHz filter (0.7 dB),
(b) one RLC Electronics F-30-8000 (0.7 dB),
(c) one Radiall r591723605 switch (0.3 dB),
(d) extra cabling (0.5 dB).

Moreover, in CD 20241206 an extra 20 dB internal attenuation is applied in the measurement instrument. On the whole, we estimate a difference in attenuation of 22.2 dB, which we add to A_3^{SQ} to obtain $A_1^{IDT} = (-78.8 \pm 2.0)$ dB, where the increased error accounts for the misestimation of the attenuation of the different components.

Similarly, we estimate the attenuation of the different components on the SQUID array resonator feedline, finding $A_1^{SQ} = (-78.8 \pm 2.0)$ dB.

CD 20240927; Here, to calibrate the input attenuation of the SQUID array resonator line, we perform a power sweep of the SQUID array resonator near zero flux. Then, we simultaneously fit several S_{21} traces for increasing power, assuming the value of self-Kerr of the bare SQUID array resonator obtained from the cross-Kerr study (Fig. 5). We find an attenuation $A_2^{SQ} = (-97.0 \pm 1.5)$ dB, where the increased error accounts for the nonidealities in the calibration process.

Finally, we obtain the attenuation of the feedline of the IDT by estimating the attenuation of the different components compared to the SQUID array resonator line. The launcher IDT input line has one extra circulator (LNF-CICIC4 8A, 0.2 dB) and some extra cabling (0.5 dB). The SQUID array feedline has an additional low-pass filter (MARKI FLP-0490, 0.7 dB). Thus, we estimate the attenuation on the IDT feedline to be $A_2{}^{IDT} = (-97 \pm 2)$ dB, where the increased error accounts for the misestimation of the attenuation of the different components.

CD 20250214; we apply the same protocol as in CD 20240927. We find $A_4{}^{SQ} = (-102.0 \pm 1.5)$ dB for the feedline of the SQUID and $A_4{}^{IDT} = (-103.6 \pm 2.0)$ dB for the feedline of the IDT.

The attenuation values estimated in the different cooldowns are summarized in Table III.

Additional measurements applying two-photon drive to the SQUID array flux line were performed in a later cooldown, **CD 20251031**. The parametric drive is applied via the flux line, and no calibration of input attenuation was performed.

APPENDIX D: MEASUREMENT DETAILS

1. Bare surface acoustic waves

a. Dissipation analysis

The SAW modes come in pairs, with one longitudinal and one transverse mode. Longitudinal modes are strongly coupled to the launcher IDT, which translates into larger κ_{ext}. The transverse modes have smaller κ_{ext} and larger κ_{int}. For convenience, we indexed all modes so that odd numbers are for longitudinal modes and even numbers are for transverse modes.

We characterize the bare SAW modes by setting the SQUID array resonator frequency far detuned from the SAW modes, for example, at zero-flux bias for which $\omega_{SQ}/2\pi \approx 4.7$ GHz. We measure the reflection signal S_{33} using the setup reported in Fig. 12 to obtain the SAW modes bare frequencies and dissipations.

In Fig. 2 of the main text, we only report the longitudinal modes that we could resolve from port 3 (launcher IDT). In Fig. 14 we also report the parameters of the transverse modes extracted from port 3 (blue and blue-green markers).

In addition, we could also identify 11 extra SAW modes by flux tuning the SQUID array resonator across the SAW modes, and measuring ports 1 and 2 (S_{21} measurements, see Fig. 3). These SAW modes are coupled to the SQUID array resonator but are not coupled to the launcher IDT. The difference in coupling is due to the different placement of the launcher and coupler IDTs along the Bragg mirror. We do not have a direct access to the dissipation rates of these extra dark modes. We set their total dissipation rates to the average of the other longitudinal (95 kHz) or transverse modes (326 kHz), shown as gray markers in Fig. 14. These values are used in Eq. (5) to perform the global fit of κ_{SQ} in Fig. 4.

b. SAW mode spacing (FSR)

The FSR of the SAW resonator is approximately equal to 8.6 MHz, and it is determined by the effective cavity length, L_c. The FSR is shown in Fig. 15. Longitudinal SAW modes are separated by 8.25 to 8.8 MHz, with the largest deviation on the edge of the mirror bandwidth due to increasing effective cavity length [16]. The transverse modes have a resonance frequency from 1.6 to 2.15 MHz higher than the longitudinal modes [60].

c. FEM simulations of modes spacial profile

An ideal SAW resonator confines the mechanical excitation along the direction of propagation, between two Bragg mirrors. However, excitations with different mode profiles that have a small transverse propagation component are

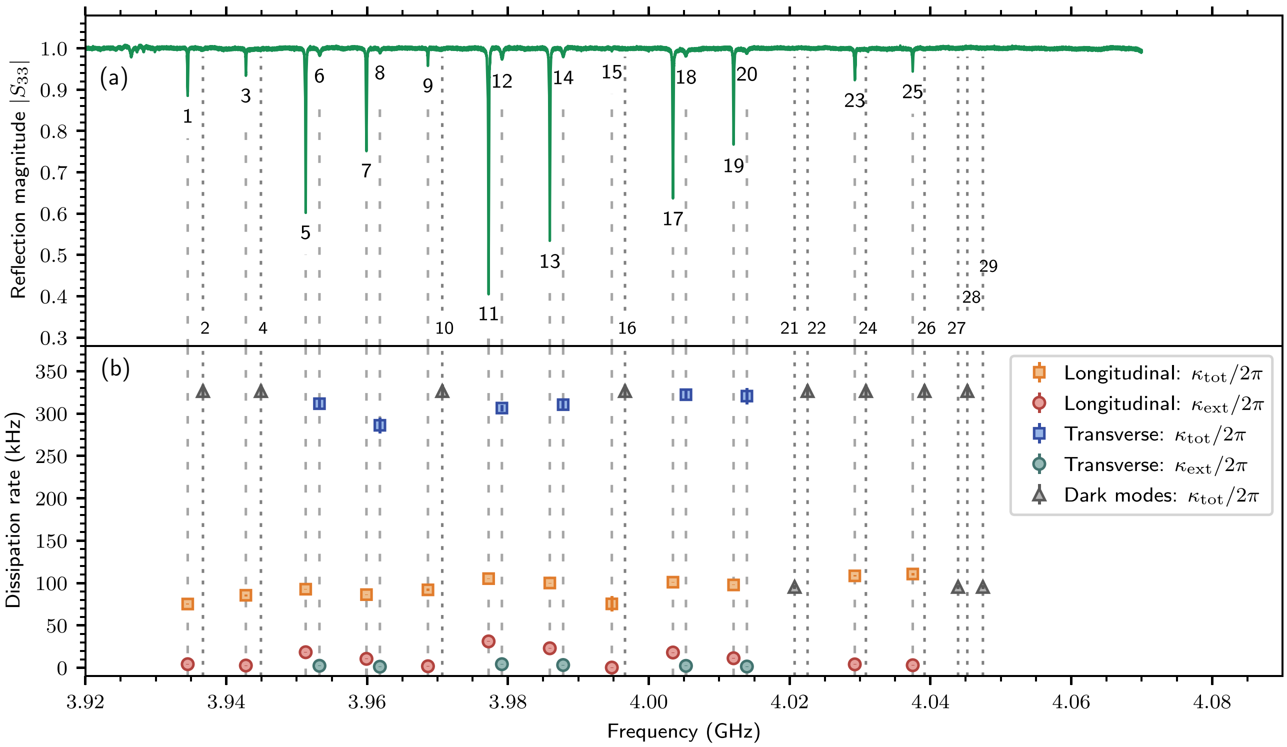

FIG. 14. Frequency and dissipation rates of bare surface acoustic wave modes. (a) Same trace S_{33} shown in Fig. 2. The SQUID array resonator is set to zero-flux point with frequency 4.7 GHz. (b) In Fig. 2 we only reported the parameters of longitudinal surface acoustic wave modes measured from the launcher IDT side (S_{33}). Here, we also report the parameters of transverse surface acoustic wave modes (blue square and blue-green circle markers) with larger internal dissipation rates. Other surface acoustic wave modes could be identified only from the SQUID array resonator side (S_{21}). We set their dissipation rates to the average value of the other modes that we could resolve directly (gray triangle markers). We use these parameters of the bare surface acoustic wave modes throughout the rest of the articles. The power of the probe tone at device level was −131 dBm.

also weakly confined and can be excited by the IDT due to its finite lateral dimensions.

Due to their mode profile, the transverse mode shows a smaller coupling to IDT and a slightly larger frequency compared to the longitudinal one. Finite element method simulations can be used to study such behavior; however, the full simulation of our geometry is very resource-intensive and is out of the scope of this work. Nevertheless, the simulation of a unit cell of the launcher (or coupler) IDT can be used to show the spatial profiles of the transverse modes.

In Fig. 16, a single finger pair with split geometry and periodic boundary conditions is used to simulate an IDT launcher. The mesh reported in panel (a) has been chosen to render every element's spatial extension smaller than the wavelength. The colorcode represents the displacement perpendicular to the substrate. In panel (b), a longitudinal mode is found at a frequency of 3.986 GHz and presents a spatial profile with a maximum at the center of the finger pair (see panel c). Higher frequency modes show a profile with one or multiple nodes, characteristic of the transverse modes. Such simulations agree qualitatively with the physical imaging of such modes on GaAs [60].

d. Dissipation versus power

We investigate the dependence of the dissipation of the bare SAW modes on the power of the input field. This measurement was performed with a vector network analyzer during the last cooldown reported in Table III. The attenuation of the line is obtained by fitting a power sweep of the SQUID array, as detailed above Sec. C 3. As shown in Fig. 17, the total dissipation decreases for increasing power, typical of the saturation of spurious two-level systems. The red dashed line corresponds to the power at which the trace shown in the main text Fig. 2 and in Fig. 14 was acquired.

e. Mechanical dissipation limitation

The propagation of SAW in anisotropic media is affected by beam steering, where the propagation direction is not perpendicular to the wave front. In a finite-size resonator, this limits the quality factor to [97]

$$Q_{\text{dif}} = \frac{5\pi}{1+\gamma}\frac{W^2}{\lambda^2}, \tag{D1}$$

where W is the width of the IDT launcher.

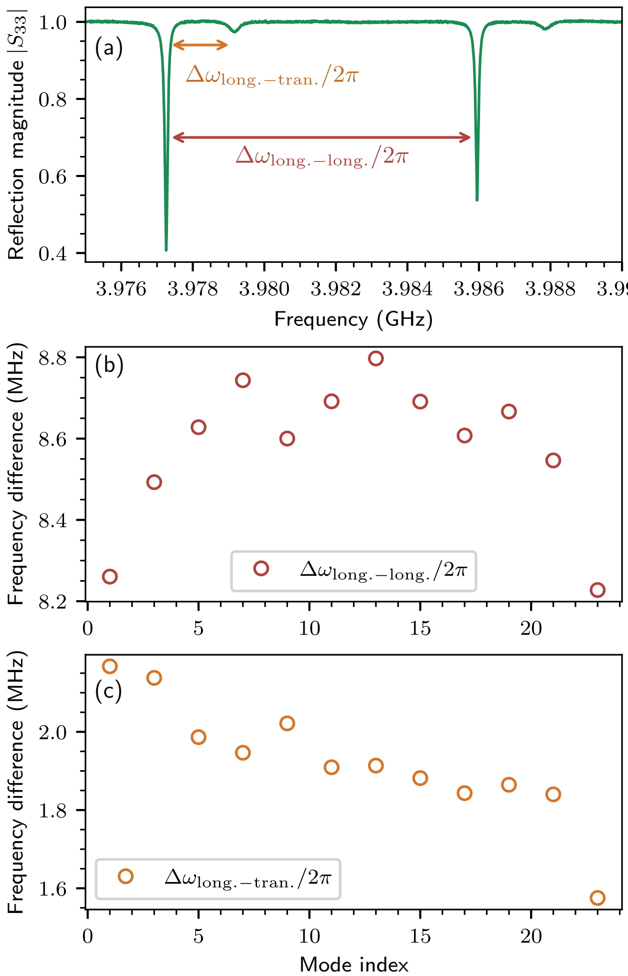

FIG. 15. Frequency difference between surface acoustic wave modes. (a) Zoom-in on the trace S_{33} of bare surface acoustic wave modes reported in Fig. 2(a). (b) and (c) From the surface acoustic wave mode positions shown in Fig. 14, we compute the frequency difference between neighboring longitudinal surface acoustic wave modes (b) and between a longitudinal mode and its neighboring transverse mode (c).

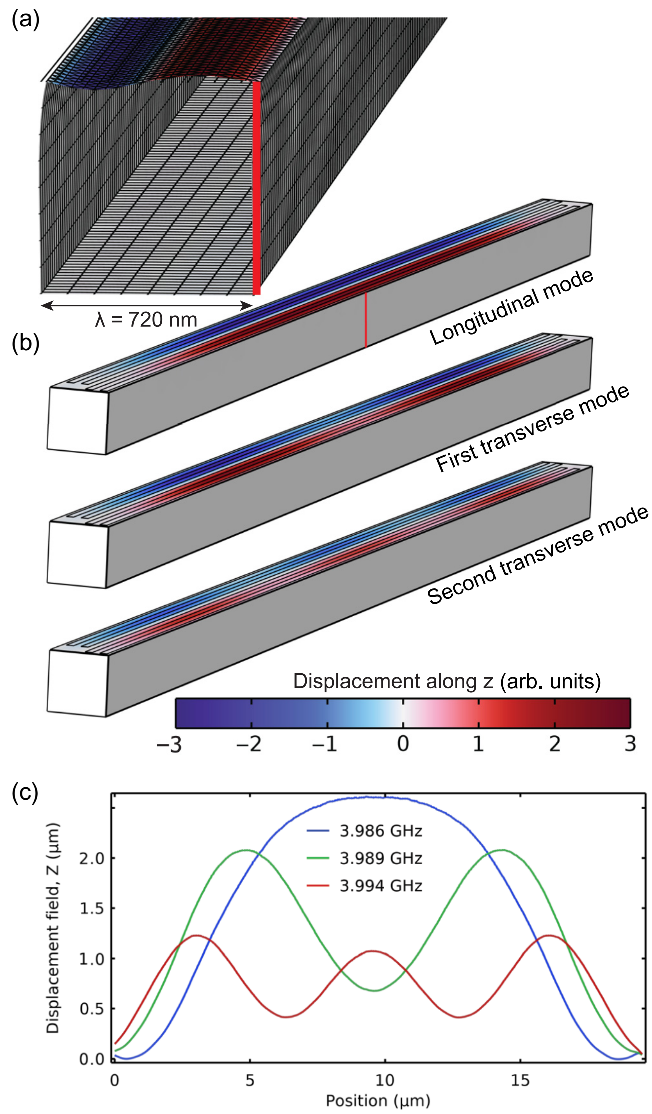

FIG. 16. Spatial profile of longitudinal and transverse modes. Finite element method simulation of the displacement in the z direction, produced by an interdigital transducer with a 1 V. In (a) a section in the center of the finger pairs show the displacement increased by a factor of 100 and the meshing elements on the surfaces. In (b) the applied voltage to each finger pair is at frequencies of 3.986, 3.989 and 3.994 GHz, exciting longitudinal, first and second transverse modes, respectively. (c) A line cut along the finger length on the surface shows the displacement for the different frequencies.

The beam steering factor γ depends on the alignment of the IDT and mirror with the propagation direction along the crystal axis [98]. We believe that the error in fabrication arises during the alignment procedure with the wafer flat. From previous devices realized on GaAs [28] and the one we realized here, we estimate $\gamma \approx -0.75 \pm 0.05$. As shown in Fig. 16, the quality factor saturates at high power to this ultimate level. We design our resonator to host a transmon qubit with the correct dimensions. Therefore, we believe that Q around 100 thousand (dissipation around 50 kHz) is the limit for this device. Future devices, with a larger aperture, can have a higher mechanical quality factor.

However, at low photon numbers, the quality factor degrades due to TLS losses. Introducing a better cleaning process will bring the quality factor closer to the diffraction limit.

2. SQUID array dissipation

a. Acoustic relaxation rate

Outside the Bragg mirror stopband, the acoustic relaxation rate of the SQUID array resonator is given

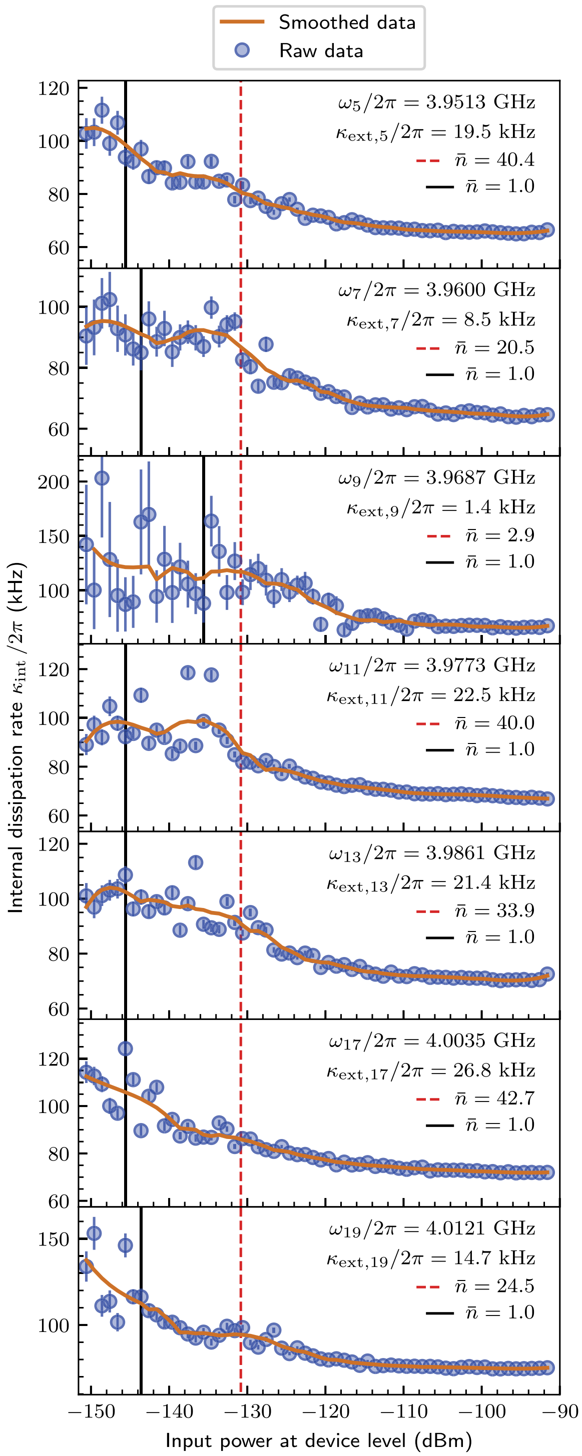

FIG. 17. Internal dissipation rate of surface acoustic wave modes as a function of input power. We measure S_{33} for increasing probe power and extract the dissipation rates by fitting each surface acoustic wave mode. Dissipation rates extracted are shown with blue markers, and the trend smoothed with a Savgol filter is shown with a solid orange line. External dissipation rates do not depend on power, and we report their values in each subplot. The input power is converted to average phonon number $\bar{n}$. The power corresponding to $\bar{n} = 1$ is shown with solid black lines, and the power used in Fig. 2 with dashed red lines.

by [45,97]

$$\Gamma(X) = \frac{1.3}{2\sqrt{2}} K^2 N_p^{\mathrm{coupler}}\, \omega_0^c \left(\frac{\sin X}{X}\right)^2, \tag{D2}$$

where $K^2 = 0.07\%$ is the effective electromechanical coupling in GaAs, $N_p^{\mathrm{coupler}} = 14$ is the number of split-finger pairs in the coupler IDT, and $X = \pi N_p^{\mathrm{coupler}}(\omega - \omega_0^c)/\omega_0^c$, with $\omega_0^c/2\pi$ the central frequency of the SAW cavity and $\omega/2\pi$ the frequency of the electromagnetic mode. In our case, the coupling results in approximately $\Gamma/N_p^{\mathrm{coupler}} \approx 2\pi \cdot 1.3$ MHz per split-finger pair.

b. SQUID array dissipation measurement

We report here the measured dissipation rates of the SQUID array resonator as a function of the bare SQUID array resonator frequency, changed via magnetic flux generated by an external superconducting coil. This measurement is performed using a vector network analyzer. For each flux value, we measure S_{21} and fit it to Eq. (B18) to obtain internal and external dissipation rates. The results are shown in Fig. 18.

The external dissipation rate of the SQUID array resonator is determined by the capacitive coupling to the $Z_0 = 50\ \Omega$ feedline. The frequency of the SQUID array resonator is tuned by changing the effective Josephson inductance using magnetic flux. We thus expect that when changing the resonance frequency of the SQUID array resonator, its external coupling rate scales as

$$\kappa_{\mathrm{ext,SQ}} = \frac{C_{\mathrm{c}}^2}{C_{\mathrm{tot}}} Z_0\, \omega_{\mathrm{SQ}}^2 = \tau\, \omega_{\mathrm{SQ}}^2, \tag{D3}$$

where C_{c} is the coupling capacitance and C_{tot} the total capacitance of the SQUID array resonator. The solid green line in Fig. 18 follows this formula with a value of $\tau = 0.31$ ps chosen to match the measured external dissipation rate around the mirror bandwidth.

Ripples in dissipation rates are observed for $\omega_{\mathrm{SQ}} > 4.2$ GHz. External dissipation rate is increased near 4.4 GHz and 4.6 GHz, while internal dissipation rate seems to increase near 4.55 GHz and 4.7 GHz. The origin of these ripples might be related to the presence of standing waves from spurious modes in the electromagnetic environment.

The internal dissipation rate can originate from two mechanisms. First, we estimate the spurious internal loss rates to be roughly constant from 3.6 GHz to 4.3 GHz with about $\kappa_{\mathrm{int}}^{\mathrm{extra}}/2\pi \approx 2$ MHz. Second, the SQUID array can emit phonons in the substrate via the coupler IDT at its capacitive end. This coupling Γ varies with the frequency following a sinc^2 profile as detailed in Eq. (D2). However, the Bragg mirrors open a gap in the phonon continuum of the substrate. Therefore, we expect this second emission channel of the SQUID array to be suppressed inside the

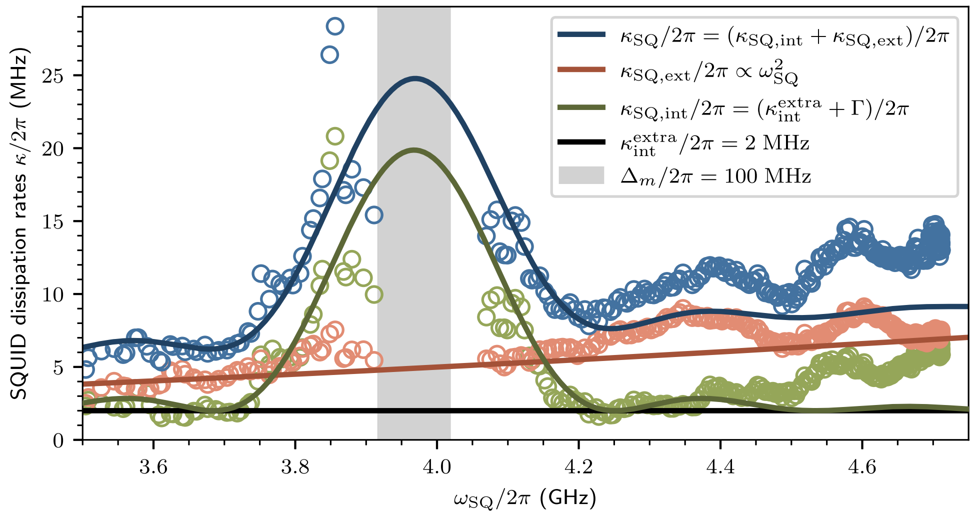

FIG. 18. Dissipation of SQUID array versus flux. We sweep the flux threading the SQUID array resonator, measure S_{21} and fit the traces with Eq. (B18) to extract the dissipation rates. Extracted values of internal (green), external (orange) and total (blue) dissipation rates are shown with markers. The internal dissipation rate from phonon emission via the coupler interdigital transducer [Γ, Eq. (D2)] is enhanced near the central frequency of the surface acoustic wave cavity $\omega_0^c/2\pi \approx 3.967$ GHz. Additional internal losses are estimated to be approximately constant at $\kappa_{\rm int}^{\rm extra}/2\pi \approx 2$ MHz near the mirror bandwidth (black line). SQUID array dissipation cannot be directly measured within the mirror bandwidth (gray shaded region astride $\omega_0^c/2\pi$). The power of the probe tone was -142 dBm, corresponding to an average photon population in the SQUID array of $\bar{n}_{\rm SQ} = 0.08$.

mirror stop band (gray shaded region in Fig. 18), except at the frequency of the bare cavity modes [16].

3. Superstrong coupling criterion for an uneven spectrum

The usual superstrong coupling regime criterion $g \gtrsim \Delta\omega$ presumes a uniform free spectral range. In our device, the spectrum is uneven: longitudinal and transverse manifolds interleave, producing local spacings that alternate between ≈ 2 MHz and ≈ 6.5 MHz. In addition, the coupler IDT is placed at approximately one-third of the cavity length, so the spatial overlap (and thus g_i) oscillates with mode index, strongly suppressing roughly every third longitudinal mode.

To enable a well-posed comparison in an uneven spectrum, we report two local, mode-resolved ratios:

(1) Mode-based ratio [one value per bare mechanical mode i, Figs. 19(a) and 19(b)]:

$$R_i \equiv \frac{g_i}{\overline{\Delta\omega i}}, \ \overline{\Delta\omega i} = \left[(\omega_i - \omega_{i-1}) + (\omega_{i+1} - \omega_i)\right]/2. \tag{D4}$$

(2) Pair-based ratio [one value per hybrid mode i connecting adjacent bare modes $i, i+1$, Figs. 19(c) and 19(d)]:

$$\tilde{R}_i \equiv \frac{\bar{g}_i}{\Delta\omega_i}, \ \bar{g}_i = \tfrac{1}{2}\left(g_i + g_{i+1}\right), \ \Delta\omega_i = \omega_{i+1} - \omega_i. \tag{D5}$$

In our device, $\overline{\Delta\omega_i}$ alternates between approximately 2 and 6.5 MHz with an average near 4 MHz. Consequently, R_i tracks the coupling envelope: strongly participating modes yield $R_i > 1$, while modes suppressed by the IDT placement give $R_i < 1$. The pair-based ratio $\tilde{R}_i$ tends to exceed unity for pairs with small $\Delta\omega_i$. As shown in Fig. 19, depending on the chosen metric, several modes have superstrong ratios exceeding unity ($\approx$ 7–8 in our dataset). Moreover, the average superstrong ratios are just slightly below one, consistent with operation at the onset of multimode (superstrong) coupling regime.

4. Hamiltonian parameter extraction

We perform a global fit of the linear RWA Hamiltonian (B14) to the resonant flux sweep shown in Figs. 3(b) and 3(c). Namely, for each flux value we extract the frequency of the resolved eigenmodes for both S_{21} and S_{33} traces. The loss function is computed globally over the entire 2D map, using the difference between the minima extracted and the eigenvalues predicted by the numerical diagonalization of the matrix T [Eq. (B3)]. The free parameters of the fit are the frequencies of the 11 SAW modes which cannot be resolved from the spectroscopy (gray markers in Fig. 14), together with the 29 coupling strengths between the electromagnetic and mechanical modes, g_i.

The fitting protocol is performed iteratively in two steps: a first general fit is performed over the full bandwidth of the mechanical cavity, as shown in Fig. 3, and then a second fit is implemented over a narrower region across the

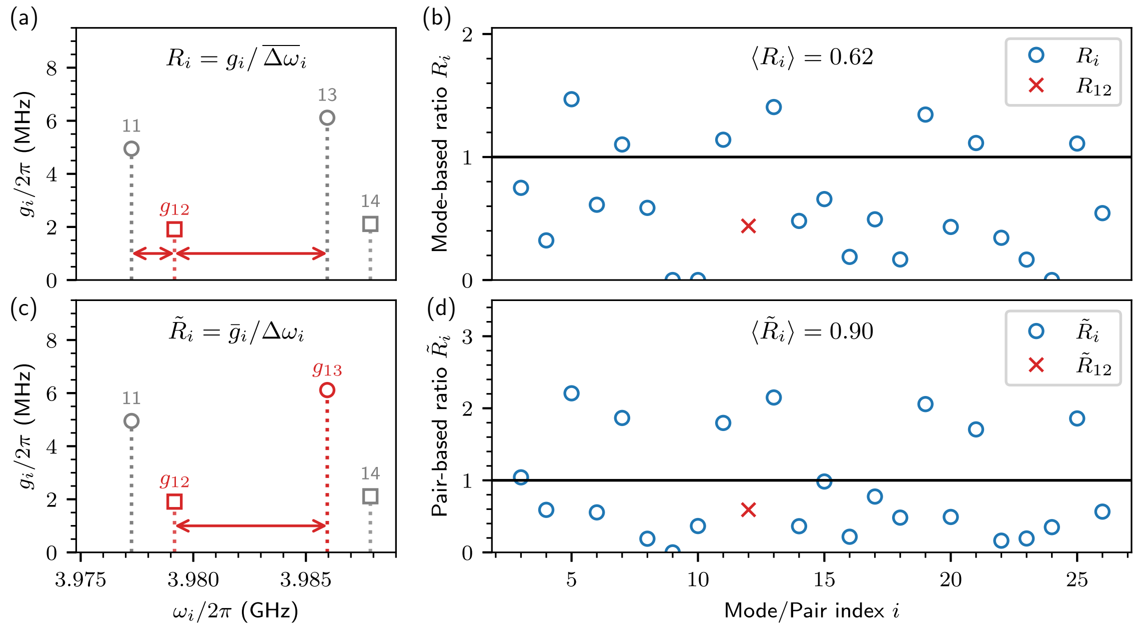

FIG. 19. Two local metrics for superstrong coupling in an uneven spectrum. (a) and (b) Mode-based ratio R_i: ratio of the surface acoustic wave-SQUID coupling g_i for bare mode i to the local average spacing $\overline{\Delta\omega_i} = \left[(\omega_i - \omega_{i-1}) + (\omega_{i+1} - \omega_i)\right]/2$. (c) and (d) Pair-based ratio $\tilde{R}_i$: ratio of the average coupling $\bar{g}_i = (g_i + g_{i+1})/2$ to the adjacent-mode spacing $\Delta\omega_i = \omega_{i+1} - \omega_i$. Red crosses in (b) and (d) mark the ratios for the modes/pairs highlighted in red in (a) and (c). Average values for each metric, $\langle R_i \rangle$ and $\langle \tilde{R}_i \rangle$, are indicated in (b) and (d), respectively.

bare SAW modes $[\omega_8; \omega_{16}]$. The second fitting step aims at refining the extraction of the parameters for the participation and the dissipation studies presented in Fig. 4. In the refined fit, the free parameters are the frequency of mode b_{16} (dark form port 3) and all the coupling strengths $[g_8; g_{16}]$. Finally, to keep consistent numbering between bare and hybridized modes, we set the couplings of the bare SAW modes b_9, b_{10}, b_{24} to zero.

5. Derivative and dissipation of hybridized modes

a. Additional data derivative and dissipation

The protocol to extract the participation of the SQUID array resonator from the derivative of the measured frequency of the hybrid modes is applied to the six hybrid modes in the range from c_{10} to c_{15}. The two bare SAW modes b_9 and b_{10} have vanishing coupling to the SQUID array resonator, $g_9 = g_{10} = 0$. Therefore, the three hybrid modes c_8, c_9 and c_{10} appear as a single continuous mode. It is the pumped mode c_p shown with pink dotted lines in Fig. 5(a), and in this section we refer to it as c_{10} for simplicity. The extended data set of Fig. 4 is displayed in Figs. 20(a), 20(c), 20(e), and 20(g), showing good agreement both from reflection and transmission data, in blue and green respectively. Modes with maximum participation below 2 % are shown as solid gray lines. The analysis of the dissipation is reported in Figs. 20(b), 20(d), 20(f), and 20(h), where the solid black line is the result of the simultaneous fit to Eq. (5) over all the modes under study, including the ones shown in Fig. 4.

A more comprehensive model of the total dissipation rate of the hybrid modes would account for interference between the external coupling rates of the bare SAW modes to the IDT, as detailed in Ref. [64]. However, in our device, the total dissipation rate of the bare SQUID array resonator is around two orders of magnitude higher than the one of the bare SAW modes. Therefore, when modes are hybridizing, their dissipation rate $\tilde{\kappa}$ is dominated by the bare SQUID array resonator contribution, so we can safely neglect possible interference effects.

The error reported on the value of κ_{SQ}, extracted from the simultaneous fit, is increased to account for the uncertainty on the participation ratios, $|u_{ij}|^2$, computed from the electromechanical coupling strengths g_i and the frequency of the bare SAW modes ω_i.

b. Extra spurious peak

We observed several weakly coupled spurious modes. To accurately extract the participation ratio of the SQUID array resonator based on the derivatives of the hybrid modes, we first characterized how the SQUID array resonator couples to these spurious modes. These modes do not follow the pattern of longitudinal and transverse modes reported in Fig. 14. These spurious modes are possibly associated with higher-order transverse excitations and appear as small avoided crossings, as shown in

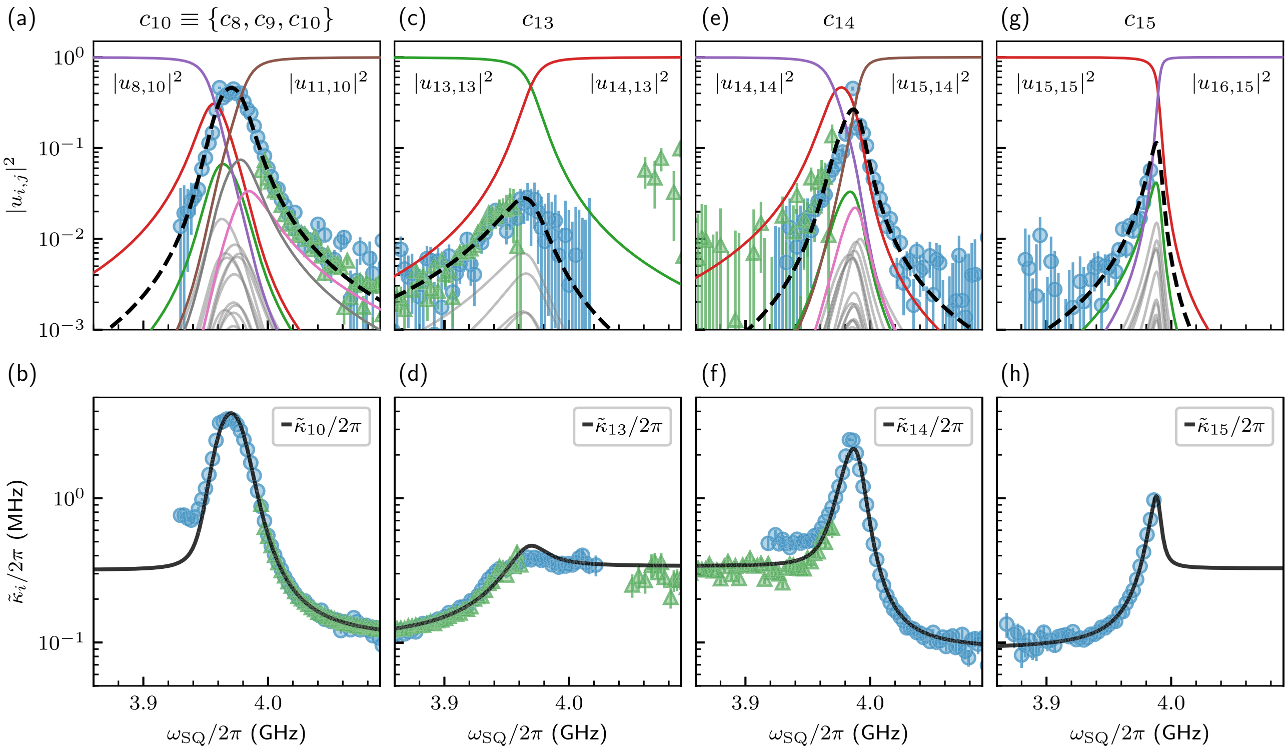

FIG. 20. Additional data for Fig. 4. Bare modes participation ratios (top row) and total dissipation rates (bottom row) for four additional hybridized modes, $\{c_{10}, c_{13}, c_{14}, c_{15}\}$. The analysis is performed on the same detailed flux sweep as shown in Figs. 4(a), 4(b).

Figs. 21(a) and 21(b) for the hybrid mode c_{12}. To track the position of these features, we fit the spectrum at each bare SQUID array resonator frequency using a double Lorentzian model,

$$L_1(\omega) + L_2(\omega) = \frac{A_1}{1 + \left(\frac{\omega - \omega_{r,1}}{\sigma_1}\right)^2} + \frac{A_2}{1 + \left(\frac{\omega - \omega_{r,2}}{\sigma_2}\right)^2}, \tag{D6}$$

where A_i are normalization factors, $\omega_{r,i}$ are the resonance frequencies, and σ_i are the half-widths at half-maximum for each Lorentzian. The coupling between the SQUID array resonator and the spurious mode is estimated by applying the same fitting protocol detailed in Sec. D 4 to the frequency of the two resonances extracted from the double Lorentzian fit, which yields $g_{spurious}/2\pi \approx 0.8$ MHz. Then, we take the derivative of the position of the resonance frequency of each Lorentzian with respect to the bare SQUID array resonator frequency [blue diamonds and crosses in Fig. 21(c)]. We find good agreement with the participation of the SQUID array resonator extracted from the numerical diagonalization of the linear model complemented with the extra peaks (orange lines).

In practice, we always use the single-peak model to extract the dissipation of the hybrid modes. However, when the data can be successfully fit with a two-peak model [see Eq. (D6)], the single-peak model fails to provide an accurate dissipation value. In these cases, we exclude the corresponding data from our dissipation analysis and use the results of the two-peak fit solely to define the exclusion regions. This procedure prevents overestimation of dissipation, as indicated by the gray markers in Fig. 21(d).

6. Self-Kerr measurements

The protocol to measure the self-Kerr of the hybrid modes consists in a resonant single-tone power sweep across the modes of interest. In Fig. 22, the self-Kerr map of the hybrid modes c_{10} to c_{15} is compared to the simulation of a driven classical Duffing oscillator as a function of the amplitude of the drive [66,68]. In the simulation all the parameters are fixed, and in particular the self-Kerr inherited by the SAW modes is derived from Eq. (6b). The theoretical curves of the model qualitatively capture the displacement of the SAW modes, until either two SAW modes start to repel each other or the mode enter the metastable region shown by the yellow and orange markers.

7. Cross-Kerr measurements

a. Measurement protocol

Cross-Kerr coefficients, $\tilde{\chi}_{i,j}$, are a quadratic correction to the linear model, which quantifies the shift in the

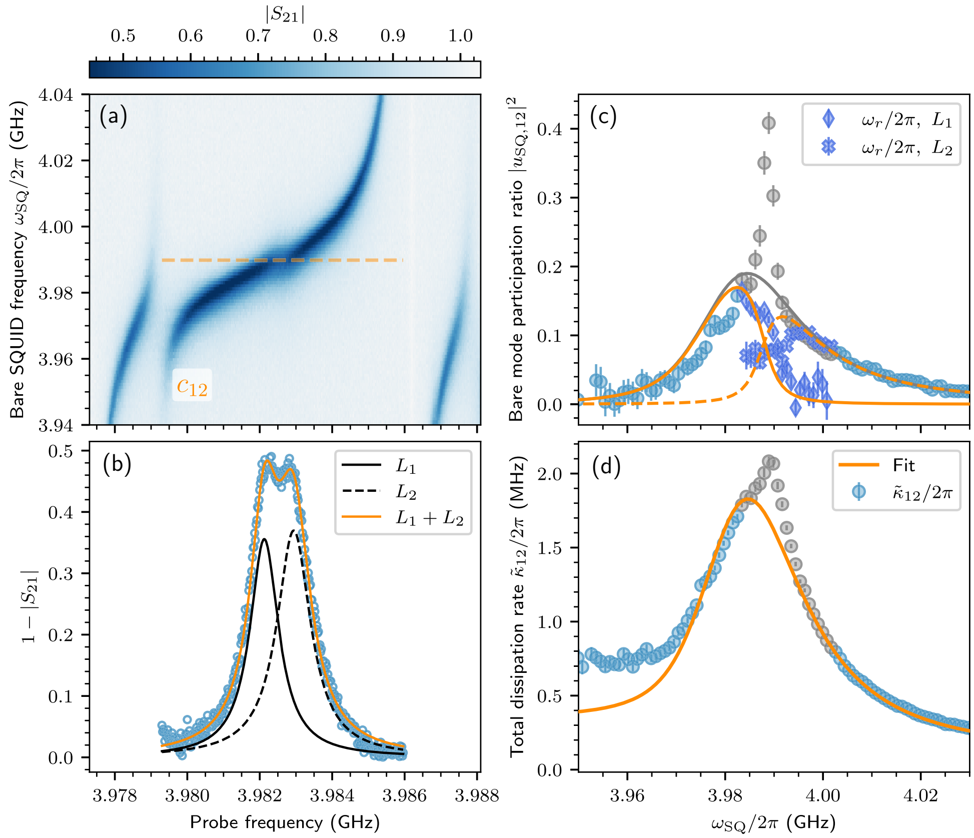

FIG. 21. Mode participation and dissipation rate analysis in presence of a spurious surface acoustic wave mode. (a) Zoom-in view of the flux sweep shown in Fig. 4(a), highlighting the presence of an additional SAW mode of bare frequency ≈ 3.983 GHz. (b) We report $1 - |S_{21}|$ at the bare SQUID array resonator frequency $\omega_{\rm SQ}/2\pi = 3.99$ GHz [orange dashed line in (a)], where the hybrid mode c_{12} is maximally hybridized with the spurious SAW mode. Measurement data are shown as blue markers. The data are fit to a double Lorentzian model [Eq. (D6)], yielding the solid orange line. The individual Lorentzian curves L_1 and L_2 are shown as black solid and dashed lines, respectively. (c) Participation of the bare SQUID array resonator in the hybridized mode c_{12} and spurious mode. Simulated participation ratios are shown for the case without the spurious mode (gray solid line) and with the spurious mode included (orange solid and dashed lines). The SQUID array resonator participation ratio is also obtained from the derivative of the measured eigenfrequencies [Eq. (4)]. Circle markers come from the same protocol described in Fig. 4, which fails in the presence of a spurious surface acoustic wave mode (gray markers). Cross and diamond blue markers are obtained from the derivative of the position of Lorentzians L_1 and L_2. (d) Dissipation rate of hybridized mode c_{12}. Circle markers are obtained from measured S_{21} using the protocol of Fig. 4. The dissipation is overestimated in the double peak region (gray) compared to the solid orange line reporting the result of the global fit of the total dissipation rates of the hybrid modes [Figs. 4(d) and 4(f)].

frequency of hybrid mode c_i as a function of the average number of excitations in hybrid mode c_j. The protocol that we adopted for measuring cross-Kerr coefficients consists of two-tone spectroscopy measurements, where we apply a pump tone on mode c_j and a weak probe tone on c_j [99]. The need to sweep the pump tone arises from the self-Kerr nonlinearity acquired by the hybrid modes, which induces a power-dependent frequency shift also in the pumped mode. As the pump power increases, this shifts the pumped mode out of resonance, necessitating an adjustment of the pump frequency to maintain resonance condition.

For every couple of hybrid modes, the dependence of the cross-Kerr on the bare SQUID array resonator frequency is obtained by first sweeping the power of the pump tone and then the flux bias applied via the external coil. For instance, the sequence in Figs. 23(b)–23(h) expands the two-tone spectroscopy map for the couple of hybrid modes (c_{12}, c_p) shown in Fig. 5(b). For this power sweep, the SQUID array resonator frequency is marked by the red dotted line in Fig. 23(a).

For the sake of simplicity, in the cross-Kerr study, we adopt the notation $c_p \in \{c_8, c_9, c_{10}\}$, since the bare modes b_9 and b_{10} are included in the numbering, but do not contribute effectively in the model as their coupling is set to zero, $g_9 = g_{10} = 0$.

Finally, the external and the total dissipation rates of the hybrid modes vary significantly as a function of the frequency of the bare SQUID array resonator. Therefore, we calibrate the power of the pump tone so that the excitation number in the pumped mode remains $\lesssim 10$ for any $\omega_{\rm SQ}$. In

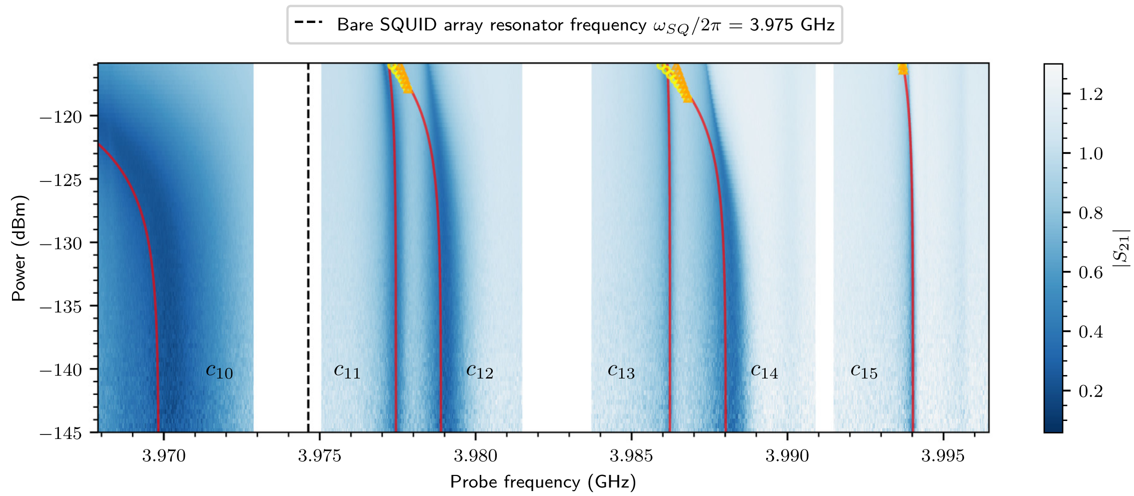

FIG. 22. Self-Kerr measurement at one flux value. Magnitude of the normalized transmission signal $|S_{21}|$ for increasing power of the probe tone. The measurement was performed around each hybrid modes individually. Red solid line shows the results of simulations for a driven classical Duffing resonator assuming the modes behave as independent oscillators. No extra fit parameters are used. The dashed black line marks the frequency of the bare SQUID array resonator ω_{SQ}. Yellow and orange markers show the region where each oscillator undergoes a bifurcation and enters a metastable region.

practice, the power of the pump tone is obtained by inverting Eq. (B20), where the frequency and dissipation rates of mode c_p as a function of ω_{SQ} are obtained from a fit of the S_{21} traces shown in Fig. 5(a) to Eq. (B18).

b. Analysis protocol

Here, to illustrate the protocol for analyzing two-tone spectroscopy maps, we focus on the pair of hybrid modes (c_{12}, c_p) . For each map in Figs. 23(b)–23(h), we extract the frequency of the probed mode c_{12} (yellow circles in Fig. 23 lower panel) as a function of the pump tone frequency, $\tilde{\omega}_{12}(f_{pump})$. To this end, we fit each S_{21} trace to the notch-type transmission signal Eq. (B18). However, because of impedance mismatch (or Fano interference), the line shape of some modes is distorted. This distortion induces a systematic offset between resonance frequency ω_r obtained from the fit to Eq. (B18) and the actual minimum in the magnitude of the measured S_{21} trace. This offset depends on the specific probed mode but is independent of the power applied to the pumped mode c_p. Therefore, to apply a uniform analysis protocol across the entire dataset, we use the minimum of the best-fit curve as the resonance frequency of the probed mode.

Subsequently, we extract the maximum negative displacement, $\Delta\tilde{\omega}^0_{12,p} := \Delta\tilde{\omega}^0_{12,p}(\bar{n}_p, \omega_{\mathrm{SQ}})$,

$$\Delta\tilde{\omega}^0_{12,p} = \min_{f_{pump}} \left(\tilde{\omega}_{12}(f_{pump})\right) - \tilde{\omega}^0_{12}, \qquad \text{(D7)}$$

where $\tilde{\omega}^0_{12}/2\pi$ is the resonance frequency of the hybrid mode c_{12} from diagonalization of the linear model Eq. (B13). In addition, the number of excitations in the pumped mode ($\bar{n}_p$) is recalibrated by using the frequency of the pump tone at maximum displacement $f_p^* = \arg\min_{f_{pump}} \left(\tilde{\omega}_{12}(f_{pump})\right)$.

The displacements, $\Delta\tilde{\omega}^0_{12,p}$, against the excitation number, $\bar{n}_p$, are then fitted to a linear model. The slope gives the cross-Kerr coefficient at the specific frequency of the SQUID array resonator considered, $\tilde{\chi}_{i,j}(\omega_{\mathrm{SQ}})$. The zero-order approximation for $\tilde{\omega}^0_{12}$ is provided by diagonalizing the linear model Eq. (B14). However, the required precision on the pump-off position of the probed modes would be below 10^{-5}. Therefore, in the linear fit we include the intercept as a fitting parameter. The dashed pink line in Fig. 23 is the pump-off frequency of the probed mode c_{12} obtained from the linear model corrected with the intercept from the fit: $\tilde{\omega}_{12} = \tilde{\omega}^0_{12} + \text{offset}$. By substituting the offset corrected frequency in Eq. (D7), we obtain $\Delta\tilde{\omega}_{12,p}$, shown in Fig. 5(c).

Finally, the uncertainty in the calibration of the line is the dominant source of error in the self- and cross-Kerr measurements, and it acts as a global rescaling of the Kerr coefficients. Therefore, we estimate its impact on the value of self-Kerr of the bare SQUID array resonator extracted from the fit as

$$\Delta\chi_{SQ,\pm} = \chi_{SQ} \times (10^{\pm\Delta A/10} - 1), \qquad \text{(D8)}$$

where ΔA is the uncertainty in the calibration of the SQUID array resonator feedline.

8. Two-photon drive measurements

Two-photon drives (also called parametric drives) are widely studied and can lead to bifurcation, bistability,

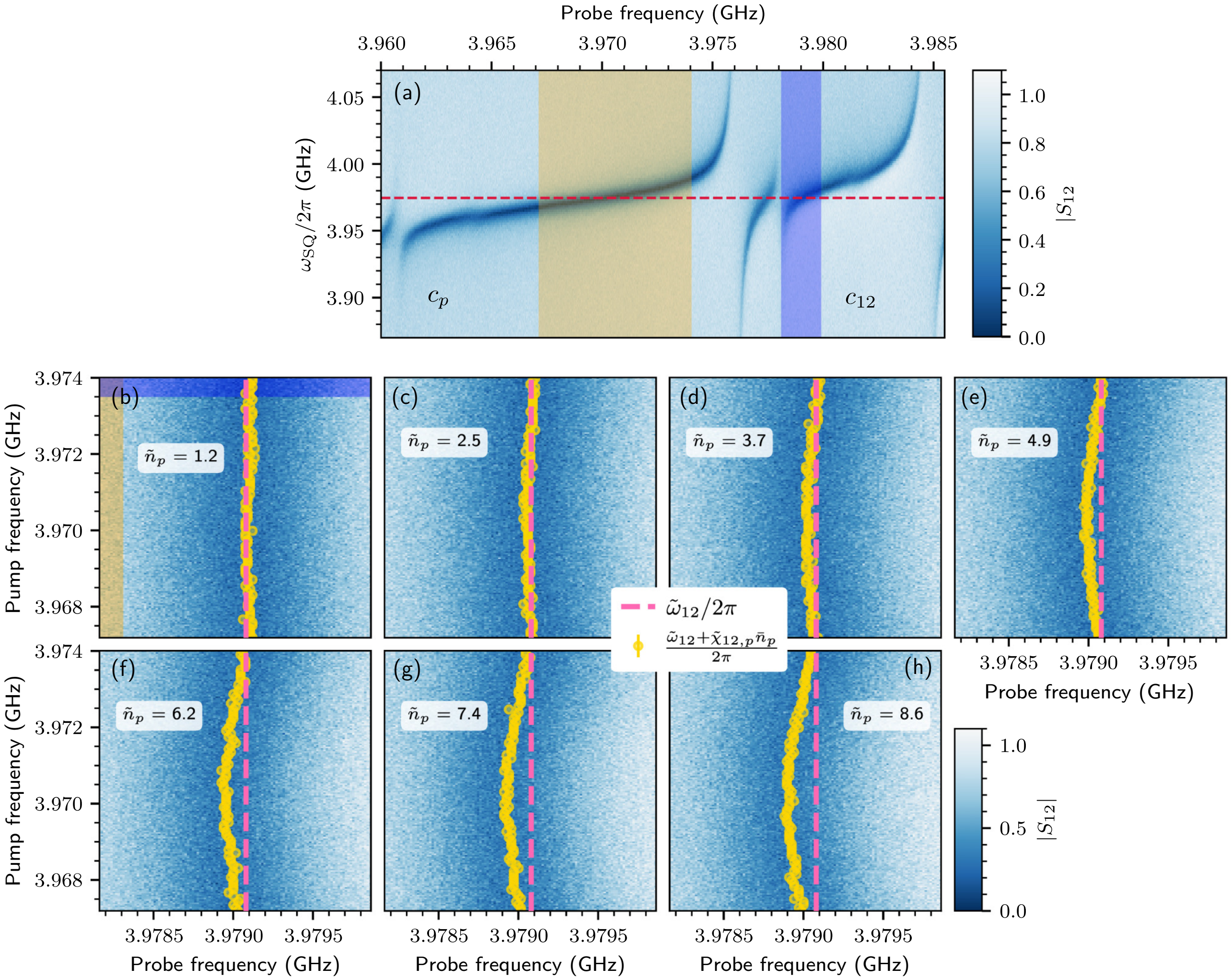

FIG. 23. Cross-Kerr measurement at one flux value. (a) Magnitude of the normalized transmission signal $|S_{21}|$ through the SQUID array resonators feedline as a function of the flux bias threading the SQUIDs loop. The dashed red line indicates the bare SQUID array resonator frequency ω_{SQ} in (b)–(h), while shaded regions highlight the frequency range of the pump tone on hybrid modes $c_p = \{c_8, c_9, c_{10}\}$ (orange) and of the probe tone on c_{12} (blue). (b)–(h) Power series of the two-tone spectroscopy maps of hybrid mode c_{12} while pumping the hybrid modes c_p. The pump power increases from left to right and from top to bottom. The shaded rectangles in (b) correspond to the shaded regions in the top panel. The dashed pink lines indicate the frequency of mode c_{12} in absence of pump tone, while the yellow circles mark the extracted resonance frequency of probed mode c_{12} for each pump frequency.

and amplification [100]. In this work we demonstrate that applying a drive at frequency $2\omega_p$ to the SQUID array flux line modulates its resonance frequency, leading to parametric down-conversion at ω_p in the SAW modes. This process is efficient when the SQUID array has a moderate detuning from the SAW modes, i.e., $\Delta \approx 1 - 10\,g$. Owing to the multimode regime, the SQUID array participation remains below a few percent in the hybrid modes, such that the downconverted excitations are mostly acoustic.

The bare SQUID array frequency is set to $\omega_{SQ}/2\pi = 3.965$ GHz. A microwave drive at frequency $2\omega_p$, close to twice a SAW mode frequency, is applied to the on-chip flux line (see Fig. 1). The applied power at room temperature is approximately -15 dBm. After waiting 500 µs, we collect the signal emitted from the launcher IDT (port 3). The signal quadratures I and Q are integrated over 15 µs and demodulated at ω_p, i.e., half the pump frequency. For the parameters used in Fig. 6, this integration time is much shorter than the typical switching time between metastable states, which is of order 10 ms. While keeping the $2\omega_p$ drive on, we collect between 1×10^5 [Fig. 6(a)] and 1.7×10^6 [Figs. 6(b) and 6(c)] data points. A short delay of 3 µs is inserted between two measurements to allow smooth data transfer without saturating the data buffer. The phase of the measured quadratures is shifted such that all the information lies along the I quadrature.

Measurements of I and Q quadratures over time are shown in Fig. 6(b) for one value of two-photon drive strength and frequency. For five pump frequency values, we construct 2D histograms of the I and Q quadratures, shown in Fig. 6(c).

We also compute the steady-state phonon number $\tilde{n}$ as $\tilde{n} = \langle I^2 + Q^2 \rangle$, where the average is taken over each time trace. The steady-state phonon number is reported in Fig. 6(a) as a function of demodulation frequency ω_p. The phonon number is reported in arbitrary units as the precise calibration of the effective gain of the output line was not performed for this measurement.

In Fig. 6 we report signal down-conversion and nonlinear parametric instability for a single hybrid mode. However, when sweeping the parametric drive frequency $2\omega_p$, we observe similar parametric effects for several hybrid modes. For a given bare SQUID array frequency, mostly hybrid modes with frequencies below the SQUID array frequency display strong parametric response. This asymmetric behavior may be caused by the negative Kerr nonlinearity of the SQUID array. A thorough study of multimode parametric instabilities is left for future studies.

[1] S. Barzanjeh, A. Xuereb, S. Gröblacher, M. Paternostro, C. A. Regal, and E. M. Weig, Optomechanics for quantum technologies, Nat. Phys. **18**, 15 (2022).
[2] B. P. Abbott, R. Abbott, T. D. Abbott, M. R. Abernathy, F. Acernese, K. Ackley, C. Adams, T. Adams, P. Addesso, R. X. Adhikari *et al.*, Observation of gravitational waves from a binary black hole merger, Phys. Rev. Lett. **116**, 061102 (2016).
[3] M. V. Gustafsson, T. Aref, A. F. Kockum, M. K. Ekström, G. Johansson, and P. Delsing, Propagating phonons coupled to an artificial atom, Science **346**, 207 (2014).
[4] G. Andersson, B. Suri, L. Guo, T. Aref, and P. Delsing, Non-exponential decay of a giant artificial atom, Nat. Phys. **15**, 1123 (2019).
[5] M. Poot and H. S. van der Zant, Mechanical systems in the quantum regime, Phys. Rep. **511**, 273 (2012).
[6] A. Clerk, K. Lehnert, P. Bertet, J. Petta, and Y. Nakamura, Hybrid quantum systems with circuit quantum electrodynamics, Nat. Phys. **16**, 257 (2020).
[7] A. Ashkin, J. M. Dziedzic, J. E. Bjorkholm, and S. Chu, Observation of a single-beam gradient force optical trap for dielectric particles, Opt. Lett. **11**, 288 (1986).
[8] W. D. Phillips and H. Metcalf, Laser deceleration of an atomic beam, Phys. Rev. Lett. **48**, 596 (1982).
[9] A. D. O'Connell, M. Hofheinz, M. Ansmann, R. C. Bialczak, M. Lenander, E. Lucero, M. Neeley, D. Sank, H. Wang, M. Weides *et al.*, Quantum ground state and single-phonon control of a mechanical resonator, Nature **464**, 697 (2010).
[10] P. Arrangoiz-Arriola, E. A. Wollack, M. Pechal, J. D. Witmer, J. T. Hill, and A. H. Safavi-Naeini, Coupling a superconducting quantum circuit to a phononic crystal defect cavity, Phys. Rev. X **8**, 031007 (2018).
[11] J. D. Teufel, T. Donner, D. Li, J. W. Harlow, M. Allman, K. Cicak, A. J. Sirois, J. D. Whittaker, K. W. Lehnert, and R. W. Simmonds, Sideband cooling of micromechanical motion to the quantum ground state, Nature **475**, 359 (2011).
[12] S. Kotler, G. A. Peterson, E. Shojaee, F. Lecocq, K. Cicak, A. Kwiatkowski, S. Geller, S. Glancy, E. Knill, R. W. Simmonds *et al.*, Direct observation of deterministic macroscopic entanglement, Science **372**, 622 (2021).
[13] Y. Chu, P. Kharel, W. H. Renninger, L. D. Burkhart, L. Frunzio, P. T. Rakich, and R. J. Schoelkopf, Quantum acoustics with superconducting qubits, Science **358**, 199 (2017).
[14] R. Manenti, A. F. Kockum, A. Patterson, T. Behrle, J. Rahamim, G. Tancredi, F. Nori, and P. J. Leek, Circuit quantum acoustodynamics with surface acoustic waves, Nat. Commun. **8**, 975 (2017).
[15] K. J. Satzinger, Y. Zhong, H.-S. Chang, G. A. Peairs, A. Bienfait, M.-H. Chou, A. Cleland, C. R. Conner, É. Dumur, J. Grebel *et al.*, Quantum control of surface acoustic-wave phonons, Nature **563**, 661 (2018).
[16] L. R. Sletten, B. A. Moores, J. J. Viennot, and K. W. Lehnert, Resolving phonon Fock states in a multimode cavity with a double-slit qubit, Phys. Rev. X **9**, 021056 (2019).
[17] A. Noguchi, R. Yamazaki, Y. Tabuchi, and Y. Nakamura, Qubit-assisted transduction for a detection of surface acoustic waves near the quantum limit, Phys. Rev. Lett. **119**, 180505 (2017).
[18] J. Chen, X. He, W. Gao, X. Liu, Z. Niu, K. Liu, W. Peng, Z. Wang, and Z.-R. Lin, On-chip integration and strong coupling between ScAlN thin-film surface acoustic wave resonators and superconducting qubits, Appl. Phys. Lett. **126**, 144001 (2025).
[19] A. Hugot, Q. Greffe, G. Julie, E. Eyraud, F. Balestro, and J. Viennot, Approaching optimal microwave-acoustic transduction on lithium niobate using SQUID arrays, Nat. Electron. **9**, 152 (2026).
[20] E. E. Wollman, C. Lei, A. Weinstein, J. Suh, A. Kronwald, F. Marquardt, A. A. Clerk, and K. Schwab, Quantum squeezing of motion in a mechanical resonator, Science **349**, 952 (2015).
[21] S. Marti, U. von Lüpke, O. Joshi, Y. Yang, M. Bild, A. Omahen, Y. Chu, and M. Fadel, Quantum squeezing in a nonlinear mechanical oscillator, Nat. Phys. **20**, 1448 (2024).
[22] Y. Chu, P. Kharel, T. Yoon, L. Frunzio, P. T. Rakich, and R. J. Schoelkopf, Creation and control of multi-phonon Fock states in a bulk acoustic-wave resonator, Nature **563**, 666 (2018).
[23] H. Qiao, É. Dumur, G. Andersson, H. Yan, M.-H. Chou, J. Grebel, C. R. Conner, Y. J. Joshi, J. M. Miller, R. G. Povey *et al.*, Splitting phonons: Building a platform for linear mechanical quantum computing, Science **380**, 1030 (2023).
[24] M. Bild, M. Fadel, Y. Yang, U. Von Lüpke, P. Martin, A. Bruno, and Y. Chu, Schrödinger cat states of a 16-microgram mechanical oscillator, Science **380**, 274 (2023).
[25] F. Pistolesi, A. N. Cleland, and A. Bachtold, Proposal for a nanomechanical qubit, Phys. Rev. X **11**, 031027 (2021).
[26] X. Han, C.-L. Zou, W. Fu, M. Xu, Y. Xu, and H. X. Tang, Superconducting cavity electromechanics: The realization

of an acoustic frequency comb at microwave frequencies, Phys. Rev. Lett. **129**, 107701 (2022).
[27] C. Samanta, S. De Bonis, C. Møller, R. Tormo-Queralt, W. Yang, C. Urgell, B. Stamenic, B. Thibeault, Y. Jin, D. Czaplewski *et al.*, Nonlinear nanomechanical resonators approaching the quantum ground state, Nat. Phys. **19**, 1340 (2023).
[28] G. Andersson, S. W. Jolin, M. Scigliuzzo, R. Borgani, M. O. Tholén, J. C. Rivera Hernández, V. Shumeiko, D. B. Haviland, and P. Delsing, Squeezing and multimode entanglement of surface acoustic wave phonons, PRX Quantum **3**, 010312 (2022).
[29] Y. Yang, I. Kladarić, M. Drimmer, U. von Lüpke, D. Lenterman, J. Bus, S. Marti, M. Fadel, and Y. Chu, A mechanical qubit, Science **386**, 783 (2024).
[30] R. G. Cortinas, Towards the generation of mechanical Kerr-cats: Awakening the perturbative quantum Moyal corrections to classical motion, New J. Phys. **26**, 023022 (2024).
[31] E. A. Wollack, A. Y. Cleland, R. G. Gruenke, Z. Wang, P. Arrangoiz-Arriola, and A. H. Safavi-Naeini, Quantum state preparation and tomography of entangled mechanical resonators, Nature **604**, 463 (2022).
[32] U. von Lüpke, I. C. Rodrigues, Y. Yang, M. Fadel, and Y. Chu, Engineering multimode interactions in circuit quantum acoustodynamics, Nat. Phys. **20**, 564 (2024).
[33] R. Manenti, M. J. Peterer, A. Nersisyan, E. B. Magnusson, A. Patterson, and P. J. Leek, Surface acoustic wave resonators in the quantum regime, Phys. Rev. B **93**, 041411(R) (2016).
[34] G. Andersson, A. L. O. Bilobran, M. Scigliuzzo, M. M. de Lima, J. H. Cole, and P. Delsing, Acoustic spectral hole-burning in a two-level system ensemble, npj Quantum Inf. **7**, 15 (2021).
[35] R. G. Gruenke-Freudenstein, E. Szakiel, G. P. Multani, T. Makihara, A. G. Hayden, A. Khalatpour, E. A. Wollack, A. Akoto-Yeboah, S. Salmani-Rezaie, and A. H. Safavi-Naeini, Surface and bulk two-level system losses in lithium niobate acoustic resonators, Phys. Rev. Appl. **23**, 064055 (2025).
[36] S. A. Tadesse and M. Li, Sub-optical wavelength acoustic wave modulation of integrated photonic resonators at microwave frequencies, Nat. Commun. **5**, 5402 (2014).
[37] J.-C. Beugnot, S. Lebrun, G. Pauliat, H. Maillotte, V. Laude, and T. Sylvestre, Brillouin light scattering from surface acoustic waves in a subwavelength-diameter optical fibre, Nat. Commun. **5**, 5242 (2014).
[38] A. Iyer, Y. P. Kandel, W. Xu, J. M. Nichol, and W. H. Renninger, Coherent optical coupling to surface acoustic wave devices, Nat. Commun. **15**, 3993 (2024).
[39] S. J. Whiteley, G. Wolfowicz, C. P. Anderson, A. Bourassa, H. Ma, M. Ye, G. Koolstra, K. J. Satzinger, M. V. Holt, F. J. Heremans *et al.*, Spin–phonon interactions in silicon carbide addressed by gaussian acoustics, Nat. Phys. **15**, 490 (2019).
[40] S. Maity, L. Shao, S. Bogdanović, S. Meesala, Y.-I. Sohn, N. Sinclair, B. Pingault, M. Chalupnik, C. Chia, L. Zheng *et al.*, Coherent acoustic control of a single silicon vacancy spin in diamond, Nat. Commun. **11**, 193 (2020).
[41] Y. Sato, Jason C. H. Chen, M. Hashisaka, K. Muraki, and T. Fujisawa, Two-electron double quantum dot coupled to coherent photon and phonon fields, Phys. Rev. B **96**, 115416 (2017).
[42] M. J. A. Schuetz, E. M. Kessler, G. Giedke, L. M. K. Vandersypen, M. D. Lukin, and J. I. Cirac, Universal quantum transducers based on surface acoustic waves, Phys. Rev. X **5**, 031031 (2015).
[43] D. Meiser and P. Meystre, Superstrong coupling regime of cavity quantum electrodynamics, Phys. Rev. A—At., Mol. Opt. Phys. **74**, 065801 (2006).
[44] N. M. Sundaresan, Y. Liu, D. Sadri, L. J. Szőcs, D. L. Underwood, M. Malekakhlagh, H. E. Türeci, and A. A. Houck, Beyond strong coupling in a multimode cavity, Phys. Rev. X **5**, 021035 (2015).
[45] B. A. Moores, L. R. Sletten, J. J. Viennot, and K. W. Lehnert, Cavity quantum acoustic device in the multimode strong coupling regime, Phys. Rev. Lett. **120**, 227701 (2018).
[46] J. Puertas Martínez, S. Léger, N. Gheeraert, R. Dassonneville, L. Planat, F. Foroughi, Y. Krupko, O. Buisson, C. Naud, W. Hasch-Guichard *et al.*, A tunable Josephson platform to explore many-body quantum optics in circuit-QED, npj Quantum Inf. **5**, 19 (2019).
[47] R. Kuzmin, N. Mehta, N. Grabon, R. Mencia, and V. E. Manucharyan, Superstrong coupling in circuit quantum electrodynamics, npj Quantum Inf. **5**, 20 (2019).
[48] Y. Y. Gao, B. J. Lester, Y. Zhang, C. Wang, S. Rosenblum, L. Frunzio, L. Jiang, S. M. Girvin, and R. J. Schoelkopf, Programmable interference between two microwave quantum memories, Phys. Rev. X **8**, 021073 (2018).
[49] W.-L. Ma, S. Puri, R. J. Schoelkopf, M. H. Devoret, S. M. Girvin, and L. Jiang, Quantum control of bosonic modes with superconducting circuits, Sci. Bull. **66**, 1789 (2021).
[50] L. Li, X. Ruan, S.-L. Zhao, B.-J. Chen, G.-H. Liang, Y. Liu, C.-L. Deng, W.-P. Yuan, J.-C. Song, Z.-H. Liu *et al.*, Quantum acoustics with superconducting qubits in the multimode transition-coupling regime, Phys. Rev. Appl. **24**, 064064 (2025).
[51] F. Lecocq, L. Ranzani, G. A. Peterson, K. Cicak, R. W. Simmonds, J. D. Teufel, and J. Aumentado, Nonreciprocal microwave signal processing with a field-programmable Josephson amplifier, Phys. Rev. Appl. **7**, 024028 (2017).
[52] N. E. Frattini, V. V Sivak, A. Lingenfelter, S. Shankar, and M. H. Devoret, Optimizing the nonlinearity and dissipation of a snail parametric amplifier for dynamic range, Phys. Rev. Appl. **10**, 054020 (2018).
[53] F. Minganti, A. Biella, N. Bartolo, and C. Ciuti, Spectral theory of Liouvillians for dissipative phase transitions, Phys. Rev. A **98**, 042118 (2018).
[54] G. Beaulieu, F. Minganti, S. Frasca, V. Savona, S. Felicetti, R. Di Candia, and P. Scarlino, Observation of first-and second-order dissipative phase transitions in a two-photon driven kerr resonator, Nat. Commun. **16**, 1954 (2025).
[55] G. Beaulieu, F. Minganti, S. Frasca, M. Scigliuzzo, S. Felicetti, R. Di Candia, and P. Scarlino, Criticality-enhanced quantum sensing with a parametric superconducting resonator, PRX Quantum **6**, 020301 (2025).

[56] G. Mihailescu, U. Alushi, R. Di Candia, S. Felicetti, and K. Gietka, Critical quantum sensing: A tutorial on parameter estimation near quantum phase transitions, arXiv:2510.02035.
[57] P. Roushan, C. Neill, A. Megrant, Y. Chen, R. Babbush, R. Barends, B. Campbell, Z. Chen, B. Chiaro, A. Dunsworth *et al.*, Chiral ground-state currents of interacting photons in a synthetic magnetic field, Nat. Phys. **13**, 146 (2017).
[58] J. Del Pino, J. J. Slim, and E. Verhagen, Non-Hermitian chiral phononics through optomechanically induced squeezing, Nature **606**, 82 (2022).
[59] D. Morgan, *Surface Acoustic Wave Filters: With Applications to Electronic Communications and Signal Processing* (Academic, Northampton, UK, 2010).
[60] M. Fisicaro, T. A. Steenbergen, Y. C. Doedes, K. Heeck, and W. Löffler, Imaging transverse modes in a gigahertz surface-acoustic-wave cavity, Phys. Rev. Appl. **23**, 014032 (2025).
[61] A. G. Del Maestro and M. J. Gingras, Quantum spin fluctuations in the dipolar Heisenberg-like rare earth pyrochlores, J. Phys.: Condens. Matter **16**, 3339 (2004).
[62] S. E. Nigg, H. Paik, B. Vlastakis, G. Kirchmair, S. Shankar, L. Frunzio, M. H. Devoret, R. J. Schoelkopf, and S. M. Girvin, Black-box superconducting circuit quantization, Phys. Rev. Lett. **108**, 240502 (2012).
[63] Z. K. Minev, Z. Leghtas, S. O. Mundhada, L. Christakis, I. M. Pop, and M. H. Devoret, Energy-participation quantization of Josephson circuits, npj Quantum Inf. **7**, 131 (2021).
[64] L. R. Sletten, *Quantum Acoustics with Multimode Surface Acoustic Wave Cavities*, Ph.D. thesis, University of Colorado at Boulder, 2021.
[65] J.-M. Raimond and S. Haroche, *Exploring the Quantum* (Oxford University, Oxford, UK, 2006), Vol. 82, p. 17.
[66] L. Peyruchat, F. Minganti, M. Scigliuzzo, F. Ferrari, V. Jouanny, F. Nori, V. Savona, and P. Scarlino, Landau–Zener without a qubit: Multiphoton sidebands interaction and signatures of dissipative quantum chaos, npj Quantum Inf. **11**, 62 (2025).
[67] M. A. Castellanos-Beltran, K. Irwin, G. Hilton, L. Vale, and K. Lehnert, Amplification and squeezing of quantum noise with a tunable Josephson metamaterial, Nat. Phys. **4**, 929 (2008).
[68] C. Eichler and A. Wallraff, Controlling the dynamic range of a Josephson parametric amplifier, EPJ Quantum Technol. **1**, 1 (2014).
[69] C. W. Sandbo Chang, C. Sabín, P. Forn-Díaz, F. Quijandría, A. M. Vadiraj, I. Nsanzineza, G. Johansson, and C. M. Wilson, Observation of three-photon spontaneous parametric down-conversion in a superconducting parametric cavity, Phys. Rev. X **10**, 011011 (2020).
[70] R. Di Candia, F. Minganti, K. Petrovnin, G. S. Paraoanu, and S. Felicetti, Critical parametric quantum sensing, npj Quantum Inf. **9**, 23 (2023).
[71] Y. Cai, X. Deng, L. Zhang, Z. Ni, J. Mai, P. Huang, P. Zheng, L. Hu, S. Liu, Y. Xu *et al.*, Quantum squeezing amplification with a weak Kerr nonlinear oscillator, Nat. Commun. **17**, 970 (2025).
[72] S. Puri, C. K. Andersen, A. L. Grimsmo, and A. Blais, Quantum annealing with all-to-all connected nonlinear oscillators, Nat. Commun. **8**, 15785 (2017).
[73] P. Álvarez, D. Pittilini, F. Miserocchi, S. Raamamurthy, G. Margiani, O. Ameye, J. Del Pino, O. Zilberberg, and A. Eichler, Biased Ising model using two coupled Kerr parametric oscillators with external force, Phys. Rev. Lett. **132**, 207401 (2024).
[74] Jimmy S. C. Hung, J. H. Busnaina, C. W. Sandbo Chang, A. M. Vadiraj, I. Nsanzineza, E. Solano, H. Alaeian, E. Rico, and C. M. Wilson, Quantum simulation of the bosonic Creutz ladder with a parametric cavity, Phys. Rev. Lett. **127**, 100503 (2021).
[75] J. J. Slim, J. del Pino, and E. Verhagen, Programmable synthetic magnetism and chiral edge states in nano-optomechanical quantum hall networks, Nat. Commun. **16**, 7471 (2025).
[76] L. Yuan, Q. Lin, M. Xiao, and S. Fan, Synthetic dimension in photonics, Optica **5**, 1396 (2018).
[77] T. Ozawa and H. M. Price, Topological quantum matter in synthetic dimensions, Nat. Rev. Phys. **1**, 349 (2019).
[78] M. Fitzpatrick, N. M. Sundaresan, Andy C. Y. Li, J. Koch, and A. A. Houck, Observation of a dissipative phase transition in a one-dimensional circuit QED lattice, Phys. Rev. X **7**, 011016 (2017).
[79] U. Alushi, A. Coppo, V. Brosco, R. Di Candia, and S. Felicetti, Collective quantum enhancement in critical quantum sensing, Commun. Phys. **8**, 74 (2025).
[80] F. Yilmaz, S. Singh, M. F. Zwanenburg, J. Hu, T. V. Stefanski, and C. K. Andersen, Energy participation ratio analysis for very anharmonic superconducting circuits, arXiv:2411.15039.
[81] J. Koch, T. M. Yu, J. Gambetta, A. A. Houck, D. I. Schuster, J. Majer, A. Blais, M. H. Devoret, S. M. Girvin, and R. J. Schoelkopf, Charge-insensitive qubit design derived from the Cooper pair box, Phys. Rev. A—At., Mol. Opt. Phys. **76**, 042319 (2007).
[82] M. Boissonneault, J. M. Gambetta, and A. Blais, Improved superconducting qubit readout by qubit-induced nonlinearities, Phys. Rev. Lett. **105**, 100504 (2010).
[83] S. Kono, J. Pan, M. Chegnizadeh, X. Wang, A. Youssefi, M. Scigliuzzo, and T. J. Kippenberg, Mechanically induced correlated errors on superconducting qubits with relaxation times exceeding 0.4 ms, Nat. Commun. **15**, 3950 (2024).
[84] I. Carusotto and C. Ciuti, Quantum fluids of light, Rev. Mod. Phys. **85**, 299 (2013).
[85] Y. Wang, J. Lee, and P. X.-L. Feng, Perspectives on phononic waveguides for on-chip classical and quantum transduction, Appl. Phys. Lett. **124**, 070502 (2024).
[86] M. Scigliuzzo, L. Peyruchat, R. M. Marabini, C. Becker, V. Jouanny, P. Delsing, and P. Scarlino, Data and code for the article “Quantum acoustics with tunable nonlinearity in the superstrong coupling regime”, 2026, https://doi.org/10.5281/zenodo.18258484
[87] P. Politzer and J. S. Murray, The Hellmann-Feynman theorem: A perspective, J. Mol. Model. **24**, 1 (2018).
[88] Q.-M. Chen, M. Partanen, F. Fesquet, K. E. Honasoge, F. Kronowetter, Y. Nojiri, M. Renger, K. G. Fedorov, A. Marx, F. Deppe *et al.*, Scattering coefficients of

superconducting microwave resonators. II. System-bath approach, Phys. Rev. B **106**, 214506 (2022).

[89] S. Probst, F. Song, P. A. Bushev, A. V. Ustinov, and M. Weides, Efficient and robust analysis of complex scattering data under noise in microwave resonators, Rev. Sci. Instrum. **86**, 024706 (2015).

[90] A. Blais, A. L. Grimsmo, S. M. Girvin, and A. Wallraff, Circuit quantum electrodynamics, Rev. Mod. Phys. **93**, 025005 (2021).

[91] G. Kirchmair, B. Vlastakis, Z. Leghtas, S. E. Nigg, H. Paik, E. Ginossar, M. Mirrahimi, L. Frunzio, S. M. Girvin, and R. J. Schoelkopf, Observation of quantum state collapse and revival due to the single-photon Kerr effect, Nature **495**, 205 (2013).

[92] J. R. Johansson, P. D. Nation, and F. Nori, QuTiP: An open-source Python framework for the dynamics of open quantum systems, Comput. Phys. Commun. **183**, 1760 (2012).

[93] K. Satzinger, C. Conner, A. Bienfait, H.-S. Chang, M.-H. Chou, A. Cleland, É. Dumur, J. Grebel, G. Peairs, R. Povey *et al.*, Simple non-galvanic flip-chip integration method for hybrid quantum systems, Appl. Phys. Lett. **114**, 173501 (2019).

[94] C. Conner, A. Bienfait, H.-S. Chang, M.-H. Chou, É. Dumur, J. Grebel, G. Peairs, R. Povey, H. Yan, Y. Zhong *et al.*, Superconducting qubits in a flip-chip architecture, Appl. Phys. Lett. **118**, 232602 (2021).

[95] J. Kitzman, J. Lane, C. Undershute, P. Harrington, N. Beysengulov, C. Mikolas, K. Murch, and J. Pollanen, Phononic bath engineering of a superconducting qubit, Nat. Commun. **14**, 3910 (2023).

[96] G. Calajó, F. Ciccarello, D. Chang, and P. Rabl, Atom-field dressed states in slow-light waveguide QED, Phys. Rev. A **93**, 033833 (2016).

[97] T. Aref, P. Delsing, M. K. Ekström, A. F. Kockum, M. V. Gustafsson, G. Johansson, P. J. Leek, E. Magnusson, and R. Manenti, Quantum acoustics with surface acoustic waves, in *Superconducting devices in quantum optics* (Springer, 2016), p. 217.

[98] A. L. Emser, B. C. Rose, L. R. Sletten, P. Aramburu Sanchez, and K. W. Lehnert, Minimally diffracting quartz for ultra-low temperature surface acoustic wave resonators, Appl. Phys. Lett. **121**, 224001 (2022).

[99] P. R. Muppalla, O. Gargiulo, S. I. Mirzaei, B. P. Venkatesh, M. L. Juan, L. Grünhaupt, I. M. Pop, and G. Kirchmair, Bistability in a mesoscopic Josephson junction array resonator, Phys. Rev. B **97**, 024518 (2018).

[100] A. Eichler and O. Zilberberg, *Classical and Quantum Parametric Phenomena* (Oxford University, Oxford, UK, 2023).